J. Plasma Physics (2004), *vol.* 70, *part* 2, *pp.* 113–142.
DOI: 10.1017/S0022377803002629 Printed in the United Kingdom

Toroidal steady states in visco-resistive magnetohydrodynamics

LEON P. J. KAMP[1] and DAVID C. MONTGOMERY[2]

[1]Department of Applied Physics, Eindhoven University of Technology, P.O. Box 513, NL-5600 MB Eindhoven, The Netherlands
(L.P.J.Kamp@tue.nl)

[2]Department of Physics and Astronomy, Dartmouth College, 6127 Wilder Laboratory, Hanover, NH 03755-3528, USA

(Received 31 August 2003)

Abstract. Previous computations concerning the allowed magnetohydrodynamic steady states of a visco-resistive magnetofluid in a toroid are extended. The current is supported by an externally imposed toroidal electric field, and a scalar resistivity and viscosity are assumed. Emphasis is on the character of the necessary velocity fields (mass flows) that toroidal geometry demands. Non-ideal boundary conditions are imposed at the toroidal boundary. One of the more interesting results to emerge is the sensitive dependence of the flow pattern on the shape of the toroidal cross-section boundary: the dipolar poloidal flow that had appeared for cross sections that were symmetric about the midplane is seen to deform continuously into a monopolar pattern for a 'D-shaped' cross section as the viscous Lundquist number M is increased. A net toroidal mass flow also develops. A boundary layer whose properties scale with fractional powers of M is also studied. The interior of the magnetofluid is approximately force-free, with current densities and magnetic fields that are nearly parallel for JET-like parameters. Steep velocity derivatives and a steep pressure drop in this boundary layer become steeper with increasing M (decreasing viscosity). The magnetic quantities do not reflect the rapid velocity and vorticity variations in the boundary layer. The maximum velocities, in the region where the viscosity is large enough for the numerics to work, are of the order of a few hundreds of centimetres per second. Measurements of velocity fields confined to the boundary layer would misrepresent the interior plasma conditions. Uncertainties in the magnetized plasma viscosity remain as an obstacle to unambiguous tests of the results in the case of real plasmas.

1. Introduction

Few practices in the theory of magnetic plasma confinement are more widespread or less critically scrutinized than the one of using ideal magnetohydrodynamics (MHD) as the mathematical framework for deciding what the possible steady states, or 'equilibria', of the plasma can be (see for example Bateman 1978; Wesson and Campbell 1997). Yet the corresponding procedure in hydrodynamics has long been known to fail. The presence of even small values of the transport coefficients, combined with the changes in boundary conditions that are mandated by non-zero viscosity, mean that the best-known hydrodynamic steady flows (pipe flow,

Poiseuille flow, Couette flow, for example) cannot be well approximated in an ideal framework. The similarity of the MHD equations and the neutral-fluid Navier–Stokes description (a special case of MHD, in fact) suggests that there may be significant parallels for electrically conducting fluids.

The intent of this article is to note some features of MHD steady states in current-carrying plasmas that result from the inclusion of finite transport coefficients and non-ideal boundary conditions, pursuing the hydrodynamic analogy. These investigations have been in progress intermittently since 1994 and the results have been presented piecemeal as they have emerged (Montgomery and Shan 1994; Bates and Lewis 1996; Montgomery et al. 1997a; Montgomery et al. 1997b; Kamp et al. 1998; Bates and Montgomery 1998; Montgomery et al. 1999; Kamp and Montgomery 2003). The present paper intends to present in a unified framework an article that can be read in a self-contained way, and to present some new additional results that have not appeared in any of the above references.

The idea that finite transport coefficients (resistivity in particular) must affect confined MHD steady states is an old one, and goes back at least to the unpublished but influential manuscript of Pfirsch and Schlüter (1962). A variety of subsequent papers have appeared over the years which have addressed the matter (see for example Grad 1967; Grad and Hogan 1970; Grad et al. 1977; Rosen and Greene 1977; Ponno et al. 2002; Throumoulopoulos and Tasso 2003). One important feature is that a resistive steady state can only be maintained against Ohmic decay by the presence of some externally-applied driving mechanism that achieves energy balance and does work on the plasma. In practice, this could be, for example, through the application of either particle beams or externally-supported electric fields. Our earlier work has assumed the latter as being the simplest to handle theoretically, and the present calculation will also rely on imposed time-independent electric fields.

We have assumed that three features of the full MHD description needed to be enforced on an equal footing. First, mechanical force balance, by means of the equation of motion, needed to be achieved pointwise. Second, Ohm's law (irrelevant for an ideal MHD steady state of the Grad–Shafranov variety) needed to be satisfied by whatever current density and electric field were present, with some basis for the choice of profile for the transport coefficients beyond simple algebraic convenience. (We cannot defend energetically the practice of choosing a resistivity profile spatial dependence, for example, solely to make the arithmetic 'come out right' (see for example Ponno et al. 2002; Throumoulopoulos and Tasso 2003).) Third, Faraday's law, which demands curl-free electric fields in the steady state, needed to be taken seriously. With a simplified but non-ideal set of boundary conditions, it turned out that the force-balance requirement could not be achieved in toroidal geometry without velocity fields, though it can easily be achieved in the straight cylinder without flow. Moreover, it turned out that the specific velocity fields that arose depended sensitively on viscosity, so that viscous effects needed to be included in the equation of motion as well as modifying the boundary conditions. A crucial role emerged for the Hartmann number, which involves a geometric mean of magnetic diffusivity and kinematic viscosity.

Such a connected sequence of requirements, not surprisingly, leads to a complicated problem—sufficiently complicated that some other desirable features that one should include for realism have so far lain out of reach. In particular, it has been necessary to assume uniform mass density and incompressible flow in order to avoid having to deal with equations of state or solve an energy equation. A second

unfortunate feature has to do with the viscosity of a magnetized plasma, the (tensor) expression for which is prohibitively complicated to use, as well as highly uncertain in magnitude (Braginskii 1965; Balescu 1988). Moreover, the geometrically complex and chemically active boundary of a typical confinement device is far too unsymmetric and complicated to be included without oversimplifications. Nonetheless, it seems desirable to take the development as far as it can go at any moment. Any future considerations for 'non-violent' controlled fusion will need to start from as accurate a version as we can muster for the state of the confined plasma.

The above-mentioned velocity fields were first identified using perturbation theory based on the assumed smallness of the velocities involved, that is for low mechanical Reynolds number (see Montgomery et al. 1997b; Kamp et al. 1998). A low Reynolds number, in turn, was justifiable by the assumption that the magnetofluid was highly viscous. The benefit of this assumption is to be able to neglect the inertial term $(\mathbf{v} \cdot \nabla)\mathbf{v}$ in the equation of motion, and to satisfy mechanical force balance by means of the viscous force alone. Thus a characteristic flow pattern emerged, seemingly somewhat independently of the shape of the toroidal boundary cross section (since it appeared both for rectangular and circular boundaries) and independently of the viscous and resistive boundary conditions imposed: a pair of counter-rotating poloidal vortices or convection cells involving mostly toroidal vorticity.

Recently, we demonstrated an ability to relax the assumption of a high viscosity using commercially available software (see the FEMLAB Reference Manual 2001; Kamp and Montgomery 2003). The primary effect of lowering the viscosity of the plasma is the appearance of a strong toroidal velocity component that appears in the flow. Eventually this toroidal flow becomes larger than the poloidal flow if the Hartmann number becomes sufficiently large, thus formally trying to approach the ideal limit that has so often been used in treatments of steady-state magnetic fusion confinement. Moreover, near the wall of the torus, lowering the viscosity leads to a narrowing layer of increasing flow speeds, i.e. a boundary layer develops.

Although large toroidal speeds develop for low viscosity values, in the geometries considered up to now, there is no net mass flow in the toroidal direction implied. In fact due to the symmetry present in the toroidal cross section, solutions are either symmetric (even parity) or anti-symmetric (odd parity) with respect to the midplane of the torus. For both the poloidal and toroidal flow fields this implies that the velocities in the upper half of the torus are necessarily opposite to those in the lower half, thus giving rise to a zero net mass flow in the toroidal direction.

One of the main purposes of the present paper is to demonstrate that as soon as the geometrical up–down symmetry across the midplane of the torus is broken (as it is in most realistic magnetic confinement vessels), the above-mentioned pair of voltage-driven counter-rotating poloidal vortices that is so typical for the high-viscosity limit can give place to just one poloidal convection cell, which for sufficiently low viscosity and fixed resistivity fills the whole cross section of the torus. Also, the toroidal velocity is not anti-symmetrical any more, resulting in a net flow of mass in the toroidal direction around the torus. Depending upon the degree of up–down asymmetry in the torus's cross section, it may require a very small value of the viscosity to enter this previously unidentified regime where the symmetry in the flow pattern becomes broken. This also means that the previously-mentioned boundary-layer behaviour for low values of the viscosity is inextricably associated with the emergence of the flow asymmetries. One main reason to explore the

consequences of varying the viscosity of the plasma keeping the resistivity fixed is the already-mentioned uncertainties with respect to its proper (tensor) expression. Lack of a sufficiently inclusive theoretical or experimental grasp of magnetized plasma viscosity may be thought of as perhaps the most severe theoretical limitation in fusion MHD at the present time.

In Sec. 2 we present the problem to be solved. In the Appendix, the relevant equations are re-expressed, for the case of axisymmetric steady states, in terms of scalar functions which are what are actually computed. Choosing values for the various parameters that correspond as closely as possible to a data set from the first tritium shot at the Joint European Torus (JET) (The JET Team 1992) in Sec. 3 we explore in detail the boundary-layer behaviour in the various mechanical variables near the wall of the torus. In Sec. 4 we demonstrate that for a toroidal cross section that has no up–down symmetry, the dipolar nature of the flow field found for high values of the viscosity will turn into a monopolar one in the low-viscosity regime. Section 5, finally, presents a discussion and conclusions.

In order to keep the numerical development manageable, we assume boundary conditions that are as simple as are compatible with the effects under consideration. The interior bounding surface of the torus we consider is idealized as a rigid, perfectly conducting wall coated with a thin layer of insulating dielectric (to permit finite, parallel electric fields at the conductor), which is, however, perfectly slippery, resulting in stress-free mechanical boundary conditions (the vanishing of the tangential viscous stress). For a couple of cases we also present results of numerical computations using no-slip (rather than stress-free) mechanical boundary conditions, and note significant differences between the consequences of the two boundary conditions.

2. Statement of the problem

2.1. Equations and geometry

The starting point for all our computations are the dimensionless MHD equations of motion (in the familiar 'Alfvénic' units) for a uniform-density, incompressible, conducting, steady-state fluid (Cowling 1958; Shercliff 1965), Ohm's law, Ampère's law, and Faraday's law, as already presented in for example Montgomery et al. (1997):

$$(\mathbf{v}\cdot\nabla)\mathbf{v} = \mathbf{J}\times\mathbf{B} - \nabla p + \nu\nabla^2\mathbf{v}, \tag{1}$$

$$\mathbf{E} + \mathbf{v}\times\mathbf{B} = \eta\mathbf{J}, \tag{2}$$

$$\nabla\times\mathbf{B} = \mathbf{J}, \tag{3}$$

$$\nabla\times\mathbf{E} = 0, \tag{4}$$

$$\nabla\cdot\mathbf{v} = 0, \tag{5}$$

$$\nabla\cdot\mathbf{B} = 0. \tag{6}$$

Here $\mathbf{v}$, p, $\mathbf{J}$, $\mathbf{B}$, and $\mathbf{E}$ are the velocity field, the scalar pressure, the electric current density, the magnetic field, and the electric field, respectively. In the dimensionless units used, where velocities are measured in units of the Alfvén speed, ν is the reciprocal of the viscous Lundquist number, M. In terms of laboratory (cgs) units, M is given by our $\nu^{-1} = M = C_{\mathrm{a}}L/\tilde{\nu}$, where C_{a} is the Alfvén speed based on a typical magnetic field, L is a characteristic length scale (for which we will take the

https://doi.org/10.1017/S0022377803002629 Published online by Cambridge University Press

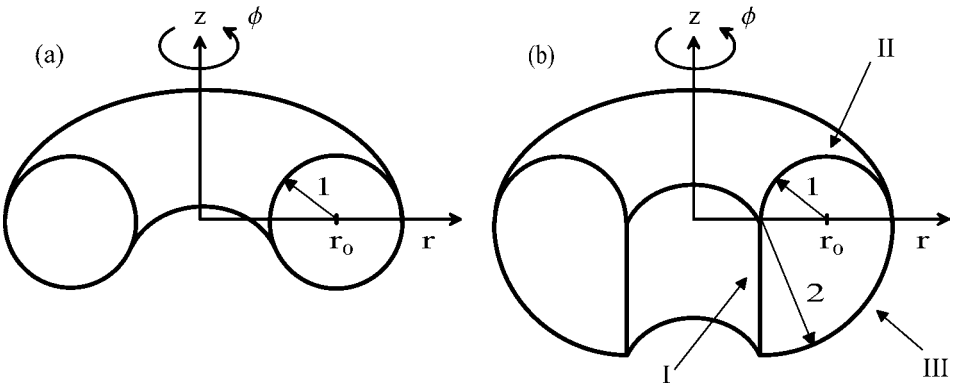

Figure 1. Geometry of the computational model. The toroid is assumed to either have a circular cross section (a) or an asymmetric, 'D'-like cross section (b).

minor radius of the torus), and $\tilde{\nu}$ is the laboratory kinematic viscosity, expressed in $\mathrm{cm}^2\ \mathrm{s}^{-1}$. η is the reciprocal of the resistive Lundquist number, S, which in laboratory units is defined by $\eta^{-1} = S = 4\pi\tilde{\sigma}C_{\mathrm{a}}L/c^2$, where $\tilde{\sigma}$ is the cgs electrical conductivity, expressed in s^{-1}, and c the speed of light. The Hartmann number H is related to M and S through the relation $H = \sqrt{MS}$.

The geometry of the model for which the above equations are solved numerically consists of an axisymmetric toroid, the axis of symmetry of which coincides with the z-axis in a set of cylindrical polar coordinates (r, ϕ, z). The boundary of the toroidal cross section is taken either to be circular (see Fig. 1(a)) or a kind of asymmetric 'D'-shape as illustrated in Fig. 1(b). The circular cross section is described by the equation (dimensionless units, again)

$$(r - r_0)^2 + z^2 = 1, \tag{7}$$

where r_0 is the ratio of the major radius of the torus and the characteristic length scale L. Since the latter is taken to be the minor radius of the torus with the circular cross section, r_0 is also identical to the aspect ratio of the torus. The asymmetric cross section depicted in Fig. 1(b) consists of a straight-line element that extends from $(r, z) = (r_0 - 1, 0)$ to $(r, z) = (r_0 - 1, -2)$, the upper half of a circle with centre in $(r, z) = (r_0, 0)$ and radius 1, and yet another segment of a circle the centre of which is in $(r, z) = (r_0 - 1, 0)$ and with radius 2. This specific asymmetric cross section is believed not to be a uniquely important one, and is chosen mainly for calculational convenience. The results derived in Sec. 4 are somewhat independent of the shape of the toroidal boundary cross section provided it is asymmetric, as has been verified by experimentation with other shapes.

The boundary conditions that are imposed upon the solutions of the set of equations (1)–(6) are that any tangential viscous stress, and the normal components of **v**, **J**, and **B**, should vanish at the walls. Occasionally, instead of the stress-free boundary condition, we will also employ the no-slip condition by requiring that the tangential component of **v** also vanishes at the walls.

The steady states described in this paper are maintained against dissipation by a curl-free, toroidal electric field the source of which is assumed to be an axisymmetric, infinitely-long, iron core that goes through the hole of the torus and through which a z-directed magnetic flux is increasing proportionally to the time. This implies

https://doi.org/10.1017/S0022377803002629 Published online by Cambridge University Press

that the imposed electric field is given by

$$\mathbf{E}_{\rm ext}(r,z) = E_0 \frac{r_0}{r} \hat{\mathbf{i}}_\varphi, \tag{8}$$

where E_0 is a reference value of the electric field at radius $r = r_0$ and $\hat{\mathbf{i}}_\varphi$ is a unit vector in the toroidal (azimuthal) direction. Additionally, a purely toroidal dc magnetic field supported by external poloidal windings around the toroid is also assumed to be present. This magnetic field is curl-free too and is described by

$$\mathbf{B}_{\rm ext}(r,z) = B_0 \frac{r_0}{r} \hat{\mathbf{i}}_\varphi, \tag{9}$$

where B_0 is a reference value of the magnetic field at radius $r = r_0$.

We will ignore the violation of electrodynamics that is implied by the presence of these finite axially symmetric electric and magnetic fields inside the perfectly conducting toroidal wall. In real life, the driving electric and magnetic fields require slits and slots cut into the perfect conductor in order that they might penetrate. That, however, would destroy the rotational symmetry desired, and make even the problem of finding steady states to perturb prohibitively difficult.

2.2. Parameter values

In order to come as close as possible to the operating regimes of current toroidal magnetic confinement devices, we choose our geometrical parameters close to those of the JET and our plasma parameters close to those of the first tritium shot in the JET (The JET Team 1992).

For the major and minor radii we take 300 cm and 150 cm respectively. The latter value is somewhere in between the horizontal minor radius (125 cm) and the vertical minor radius (200 cm) of the JET. Taking the characteristic scale length L equal to the minor radius, that is 150 cm, $r_0 = 2$ is found. The root mean square value of toroidal magnetic field is taken to be 28 kG. For the circular cross section this can be achieved by the dimensionless $B_0 = 0.94$ and for the asymmetric cross section by $B_0 = 0.87$. The value of the toroidal loop voltage is chosen somewhat arbitrarily to be 1 V, resulting in an externally applied electric field $E_0 = 2.5 \times 10^{-9}$ for the dimensionless units used. The value of the resistive Lundquist number S is chosen to give a plausible toroidal current of 3.1 MA. For the circular cross section we are led to $S = 1.11 \times 10^8$ and for the asymmetric cross section to $S = 6.92 \times 10^7$.

The plasma is assumed to be deuterium, with an electron and ion density both of 3.6×10^{13} cm^{-3} and an electron temperature of 10 keV. The ion temperature is assumed to be 18 keV. Following the tabulated formulas in the NRL Plasma Formulary (Book 1987) for collision times and transport coefficients, this gives too large a value of S (1.4×10^{10}), and we are led instead to the above-mentioned values, in order to achieve the 3.1 MA toroidal current. These lower values of S may be attributed to an anomalous resistivity, outside the MHD framework. The typical strength of the magnetic field (28 kG) and the assumed ion number density result in an Alfvén speed $C_{\rm a}$ of 7.2×10^8 cm s^{-1}.

The viscosity of a hot plasma such as those used in tokamak confinement devices is highly uncertain within orders of magnitude, experimentally and theoretically. Convincing theoretical Chapman–Enskog calculations exist, but only in the short mean free path limit, not strictly applicable to tokamak plasmas (Braginskii 1965; Balescu 1988). These calculations have been carried out with and without including the effects of a strong magnetic field on the particle collisions. Only in the

unmagnetized case does a scalar Newtonian viscosity term of the type appearing in (1) result. For the strong magnetic field case, a complicated viscous stress tensor results, with different viscosity coefficients that span about twelve orders of magnitude. If one takes the largest viscosity coefficient (the 'ion parallel' viscosity) from this set, or chooses the unmagnetized result, the kinematic viscosity can be estimated as an ion mean free path times an ion thermal speed. This leads to a laboratory kinematic viscosity $\tilde{\nu}$ of $1.25 \times 10^{15}\ \mathrm{cm}^2\ \mathrm{s}^{-1}$. The resulting viscous Lundquist number is then $M = 8.64 \times 10^{-5}$. Obviously we must regard the situation as an unsatisfactory one of considerable uncertainty, which can be resolved only when much more reliable and detailed measurements of viscous effects in tokamaks have been made. In the next two sections we will take $M = 8.64 \times 10^{-5}$ as a *lower bound* on the viscous Lundquist number and explore what happens to the flow fields if M is increased above this lower bound keeping all other parameters fixed to the above-mentioned values.

3. Boundary layer behaviour

Starting from the set of non-ideal MHD equations (1)–(6) and using the fact that we consider axisymmetric steady states, in the Appendix we derive a set of coupled, nonlinear, Poisson-like equations for the following scalar variables (see (A 7), (A 9), (A 10), (A 12), (A 13), and (A 14)): the stream function ψ, the toroidal vorticity ω_φ, the (self-consistent) toroidal magnetic field B_φ, the toroidal velocity v_φ, and the magnetic flux function χ. As is explained in the Appendix, solutions for $\mathbf{v}$, $\mathbf{B}$, and $\mathbf{J}$ can be calculated without *a priori* knowledge of the pressure p and the self-consistent electric fields (that are described by an electric potential Φ). This set of equations is solved numerically using a commercially available software package called FEMLAB (see the FEMLAB Reference Manual 2001). FEMLAB applies the finite-element method to our system of partial differential equations in two dimensions in conjunction with adaptive meshing and error control. A numerical solver that is specialized in solving stationary nonlinear equations is used.

Since in the present section the cross section of the torus is taken to be circular and symmetric with respect to the midplane of the torus (see (7)), all solutions have to be either symmetric (even parity) or anti-symmetric (odd parity) with respect to the $z = 0$ plane. B_φ, χ, and J_φ are even functions of z whereas ψ, ω_φ, and v_φ are odd functions of z. Therefore by considering only, say, the upper half of the toroid we can reduce the amount of numerical calculation by a factor of two. In a typical run the upper half of the toroidal cross section is divided into approximately 10 000 triangles with 5000 nodes to acquire the desired accuracy. In the Appendix we formulate the boundary conditions based on the symmetry properties of the various variables to be imposed for $z = 0$ (see (A 28)) and for the remaining (semicircular) boundary in case of stress-free (see (A 29)) or no-slip boundary conditions (see (A 30)).

In the present section we will assume stress-free mechanical boundary conditions as prescribed by (A 29) unless otherwise indicated. In Figs. 2 and 3 we show typical examples of a run of FEMLAB with M taken to be 8.64×10^{-5}. We reiterate that because of the symmetries about the midplane $z = 0$, we are showing only the upper half of the toroidal cross section in these and similar figures of the present section; the variables in the lower half can be inferred from obvious symmetries. Contour plots of the magnetic flux function χ (Fig. 2) and the poloidal electric

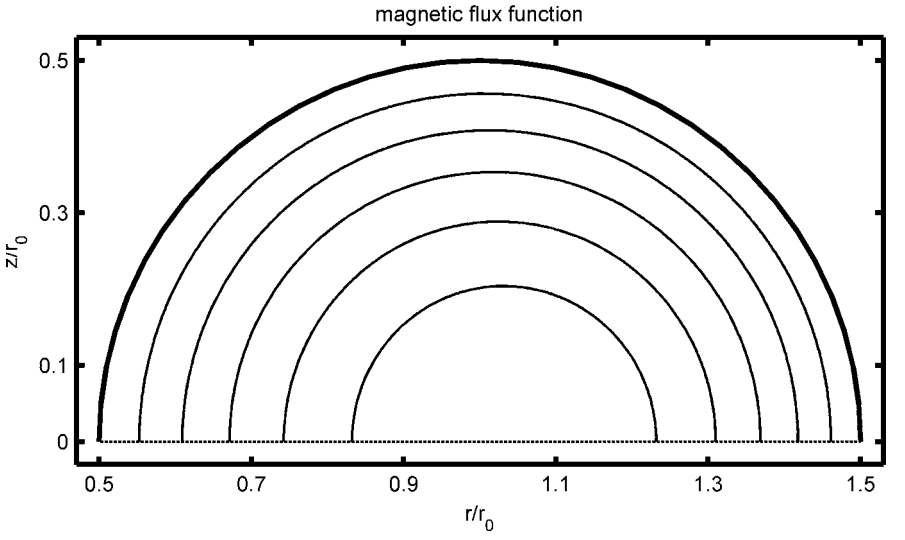

Figure 2. A plot of the poloidal magnetic field lines $M = 8.64 \times 10^{-5} \equiv M_{\rm low}$. Stress-free boundary conditions are assumed.

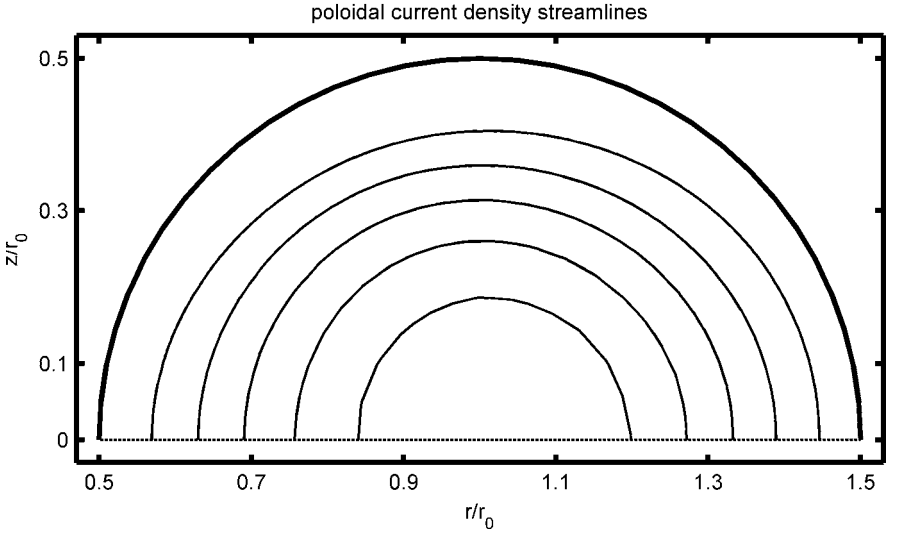

Figure 3. Streamlines of the poloidal electric current density for $M = 8.64 \times 10^{-5} \equiv M_{\rm low}$. Stress-free boundary conditions are assumed.

current density stream function rB_φ (Fig. 3) appear in these two figures. Note the slight outward shift of the magnetic surfaces with respect to the centre of the toroidal cross section. This is not too different from the 'Shafranov shift' found in ideal MHD equilibria.

Figure 4 contains a vector plot of ∇p calculated from (A 15). At the toroidal boundary, ∇p has a finite (be it small) tangential component, indicating that the

https://doi.org/10.1017/S0022377803002629 Published online by Cambridge University Press

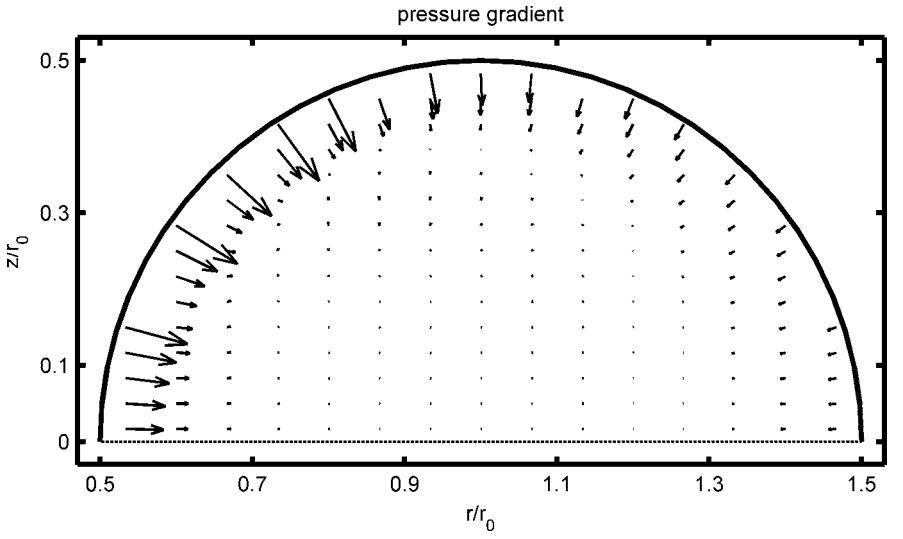

Figure 4. Vector plot of ∇p for $M = 8.64 \times 10^{-5} \equiv M_{\rm low}$. Stress-free boundary conditions are assumed.

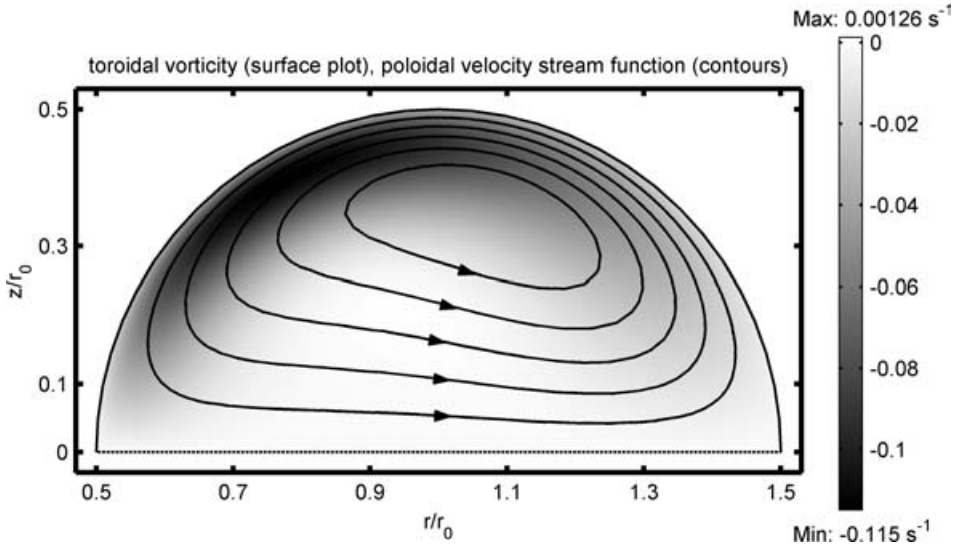

Figure 5. Surface plot of the (dimensional) toroidal vorticity ω_φ combined with contours of the poloidal velocity stream function ψ with $M = 8.64 \times 10^{-5}$. The grey-scale bar indicates the dimensional value of the toroidal vorticity in s^{-1}. Stress-free boundary conditions are assumed.

bounding wall is not an isobaric surface. However, note that the tangential viscous stress at the boundary is absent since we require stress-free boundary conditions.

The next set of figures is devoted to the behaviour of the mechanical variables for increasing values of the viscous Lundquist number M. We show combinations of contour and surface plots of the poloidal velocity stream function ψ, the toroidal vorticity ω_φ, and the toroidal velocity v_φ for $M = 8.64 \times 10^{-5} \equiv M_{\rm low}$ (Figs. 5 and 6),

https://doi.org/10.1017/S0022377803002629 Published online by Cambridge University Press

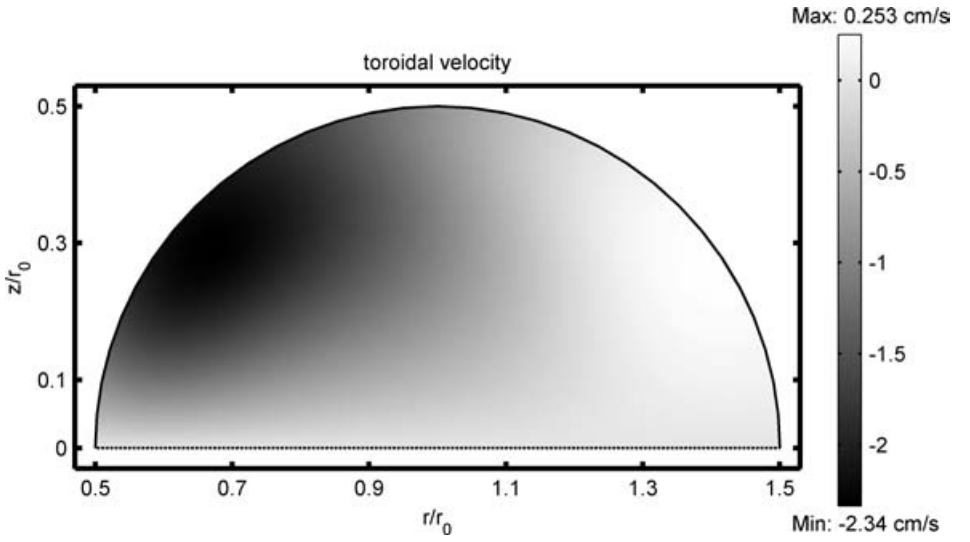

Figure 6. Surface plot of the (dimensional) toroidal velocity v_φ with $M = 8.64 \times 10^{-5}$. The grey-scale bar indicates the dimensional value of the toroidal velocity in $\mathrm{cm\,s^{-1}}$. Stress-free boundary conditions are assumed.

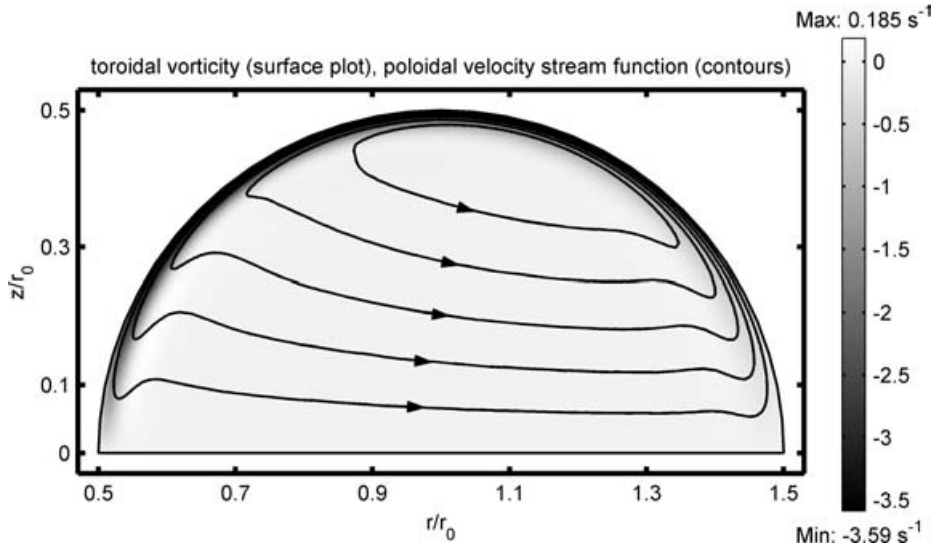

Figure 7. Same as Fig. 5 but with $M = 8.64 \times 10^{-2}$.

$M = 10^3 \times M_{\mathrm{low}}$ (Figs. 7 and 8), $M = 10^5 \times M_{\mathrm{low}}$ (Figs. 9 and 10), and $M = 10^7 \times M_{\mathrm{low}}$ (Figs. 11 and 12).

In all these plots the various shades of grey are measures for the value of the relevant toroidal quantity as is indicated by the bars that appear in these figures. The most remarkable overall feature that these plots demonstrate is the development of what essentially is a boundary layer near the interior wall of the torus when viscosity is lowered. Although the speeds (toroidal as well as poloidal) in the

https://doi.org/10.1017/S0022377803002629 Published online by Cambridge University Press

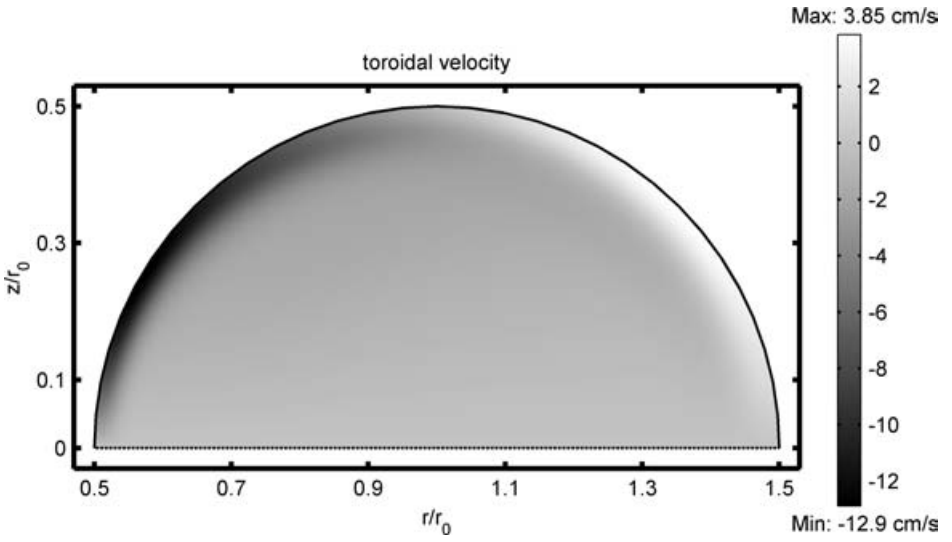

Figure 8. Same as Fig. 6 but with $M = 8.64 \times 10^{-2}$.

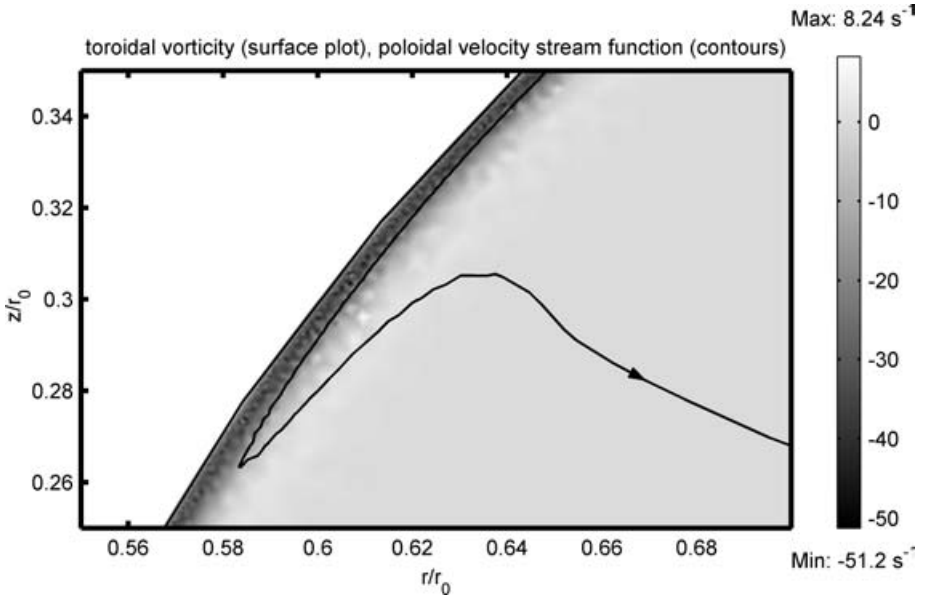

Figure 9. Same as Fig. 5 but with $M = 8.64$. Only an enlarged cut-out of the cross section is shown in order to resolve the structure of the boundary layer.

interior of the torus do not change much for increasing viscous Lundquist number (of the order of a few centimetres per second), near the wall a narrowing layer with increasing flow speeds develops. In this boundary layer large gradients in the mechanical variables ψ, ω_φ, and v_φ occur. In order to keep this narrowing boundary layer visible for $M = 8.64$ and $M = 864$, we show in Figs. 9–12 only a fraction of the total upper half of the circular cross section. This cut-out is centred around $r = 0.6r_0$ and $z = 0.3r_0$. The overall flow pattern in the torus may be inferred from

https://doi.org/10.1017/S0022377803002629 Published online by Cambridge University Press

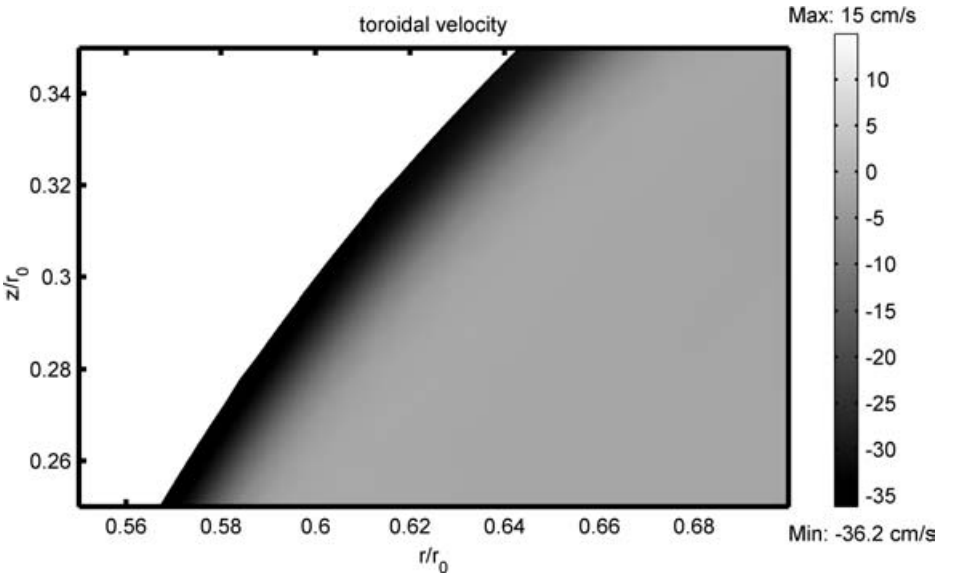

Figure 10. Same as Fig. 6 but with $M = 8.64$. Only an enlarged cut-out of the cross section is shown in order to resolve the structure of the boundary layer.

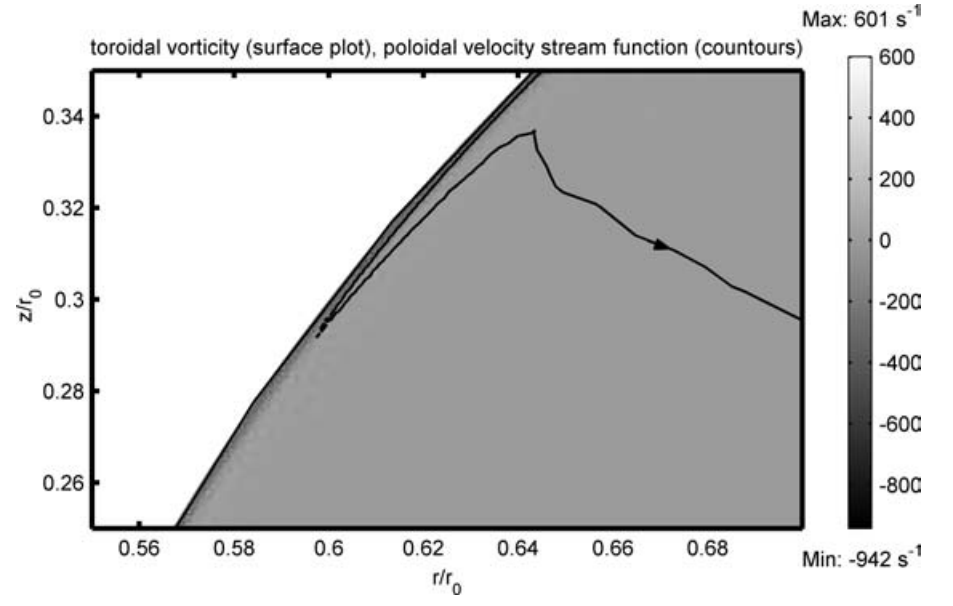

Figure 11. Same as Fig. 9 but with $M = 864$.

the fact that the topology of the flow field for these values of the viscous Lundquist numbers do not differ from those depicted in the Figs. 5–8 for the lower values of the Lundquist number. Resolving the ever-increasing fine structure of the flow field near the wall of the torus when the viscosity is lowered is what essentially limits our

https://doi.org/10.1017/S0022377803002629 Published online by Cambridge University Press

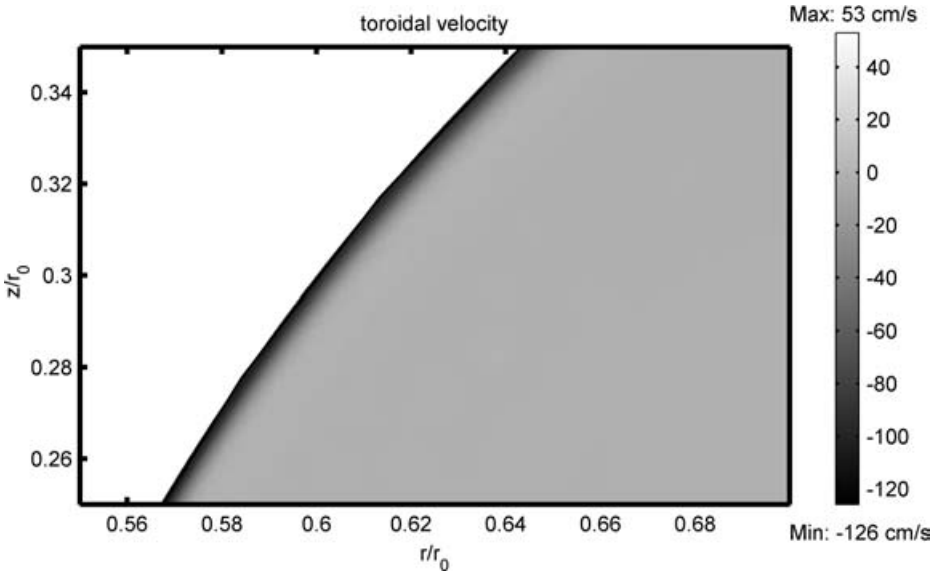

Figure 12. Same as Fig. 10 but with $M = 864$.

numerical capability to perform computations for even larger values of the viscous Lundquist number.

In order to determine the scaling of the mechanical variables and the width of the boundary layer with the viscosity of the plasma, we numerically evaluate the following cross-section line integrals:

$$V_{\rm p}(d) \equiv \frac{I_{\rm b} C_{\rm a}}{r_0} \left(\frac{1}{2\pi\rho} \oint_{C(\rho)} \|\nabla\psi \times \nabla\phi\|^2 \, ds \right)^{1/2}, \tag{10}$$

$$V_{\rm t}(d) \equiv \frac{I_{\rm b} C_{\rm a}}{r_0} \left(\frac{1}{2\pi\rho} \oint_{C(\rho)} {v_\varphi}^2 \, ds \right)^{1/2}, \tag{11}$$

$$\Omega_{\rm t}(d) \equiv \frac{C_{\rm a}}{{r_0}^2 L} \left(\frac{1}{2\pi\rho} \oint_{C(\rho)} {\omega_\varphi}^2 \, ds \right)^{1/2}. \tag{12}$$

Here, $C(\rho)$ is the circle $(r - r_0)^2 + z^2 = \rho^2$, where $0 < \rho_0 < \rho \leqslant 1$ and d is the dimensional radial distance from the wall of the torus, i.e. $d = L(1 - \rho)$. In fact, the line integrals (10), (11) and (12) denote root mean (averaged over $C(\rho)$) square values of respectively the dimensional poloidal velocity (in $\mathrm{cm\,s^{-1}}$), the toroidal velocities (in $\mathrm{cm\,s^{-1}}$) and the toroidal vorticity (in $\mathrm{s^{-1}}$). Figures 13, 14, and 15 show plots of $V_{\rm p}$, $V_{\rm t}$, and $\Omega_{\rm t}$ respectively as functions of d for different values of the viscous Lundquist number M. Since we choose $C(\rho)$ close to the circular boundary of the cross section, the development of the boundary layer as the viscosity of the plasma becomes smaller and smaller is clearly exhibited. Whereas typical flow speeds in the interior of the torus are of the order of a few centimetres per second, Figs. 12 and 13 show toroidal and poloidal speeds in excess of $100\,\mathrm{cm\,s^{-1}}$ close to the wall for the lowest value of the viscosity considered.

The scaling of the boundary-layer thickness with the viscous Lundquist number M is investigated by determining the radial distances $d = \delta_1$, $d = \delta_2$, and $d = \delta_3$

https://doi.org/10.1017/S0022377803002629 Published online by Cambridge University Press

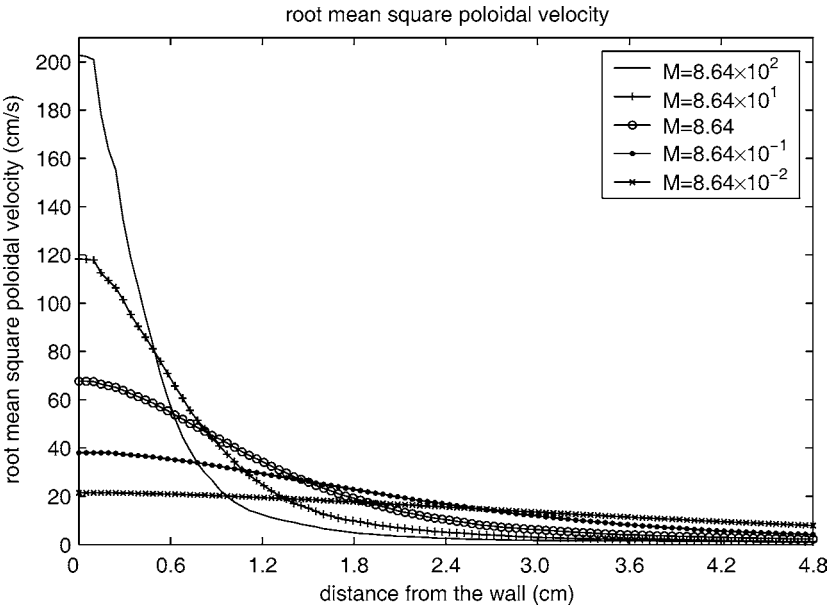

Figure 13. Root mean square value of the poloidal velocity close to the wall of the torus, i.e. inside the boundary layer, for different values of M. Stress-free boundary conditions are assumed.

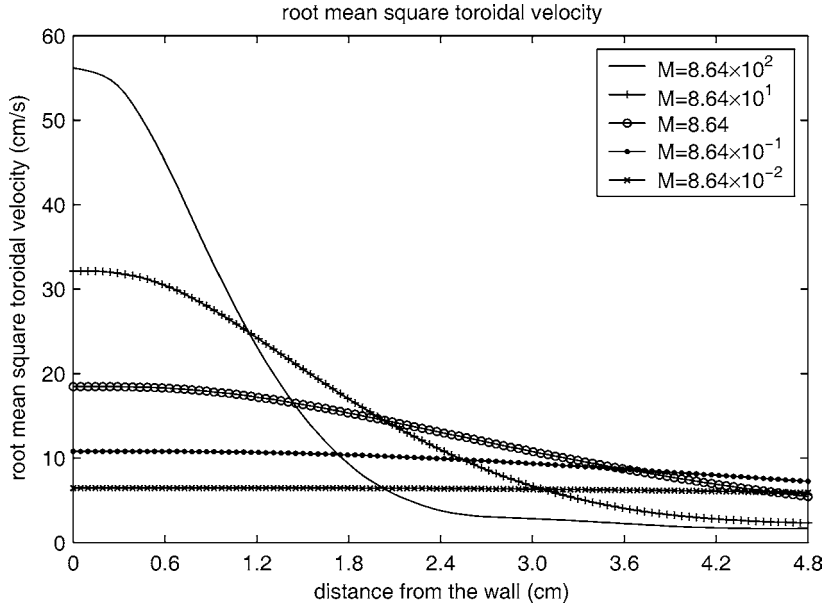

Figure 14. Root mean square value of the toroidal velocity close to the wall of the torus, i.e. inside the boundary layer, for different values of M. Stress-free boundary conditions are assumed.

https://doi.org/10.1017/S0022377803002629 Published online by Cambridge University Press

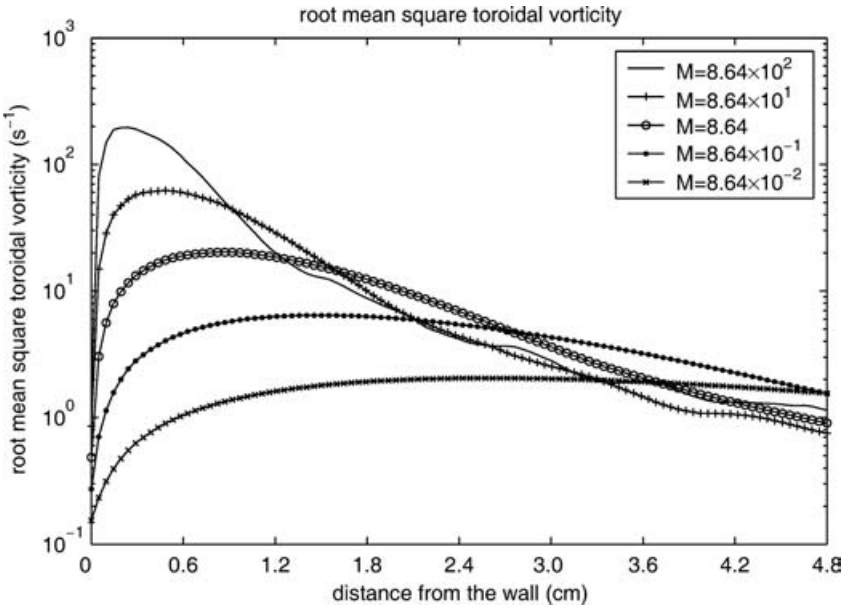

Figure 15. Root mean square value of the toroidal vorticity close to the wall of the torus, i.e. inside the boundary layer, for different values of M. Stress-free boundary conditions are assumed.

Table 1. Scaling of the width of the boundary layer and the root mean square values of the poloidal and toroidal velocities as well as the toroidal vorticity for decreasing viscosity. $\dot{\Omega}_t(\delta_3)$ denotes the derivative of $\Omega_t(d)$ with respect to d for $d = \delta_3$.

				$\frac{V_p(0)}{V_p(\delta_1)} = 2$	$\frac{V_t(0)}{V_t(\delta_2)} = 2$	$\dot{\Omega}_t(\delta_3) = 0$
M	δ_1 (cm)	δ_2 (cm)	δ_3 (cm)	$V_p(0)$ (cm s^{-1})	$V_t(0)$ (cm s^{-1})	$\Omega_t(\delta_3)$ (s^{-1})
8.64×10^{-5}	20.3	92.5	13.5	3.61	1.20	7.19×10^{-2}
8.64×10^{-4}	11.8	64.2	7.8	6.70	2.45	2.15×10^{-1}
8.64×10^{-3}	6.7	29.4	4.5	12.06	3.99	6.58×10^{-1}
8.64×10^{-2}	3.8	13.1	2.6	21.49	6.47	2.05×10^{0}
8.64×10^{-1}	2.2	6.5	1.5	38.10	10.79	6.43×10^{0}
8.64×10^{0}	1.2	3.4	0.9	67.67	18.47	2.03×10^{1}
8.64×10^{1}	0.7	1.9	0.5	118.22	32.15	6.21×10^{1}
8.64×10^{2}	0.4	1.0	0.3	202.57	56.12	1.96×10^{2}

where respectively the root mean square poloidal velocity ($V_p(d)$) has dropped to half of its value at the wall (see Fig. 13), the root mean square toroidal velocity ($V_t(d)$) has dropped to half of its value at the wall (see Fig. 14), and the root mean square toroidal vorticity ($\Omega_t(d)$) attains its extremum (see Fig. 15). The distances thus obtained are listed for the various values of the viscous Lundquist number in Table 1. Also in Table 1 we have listed the values of the root mean square values of the poloidal and toroidal velocities right at the wall, i.e. for $d = 0$, as well as the

https://doi.org/10.1017/S0022377803002629 Published online by Cambridge University Press

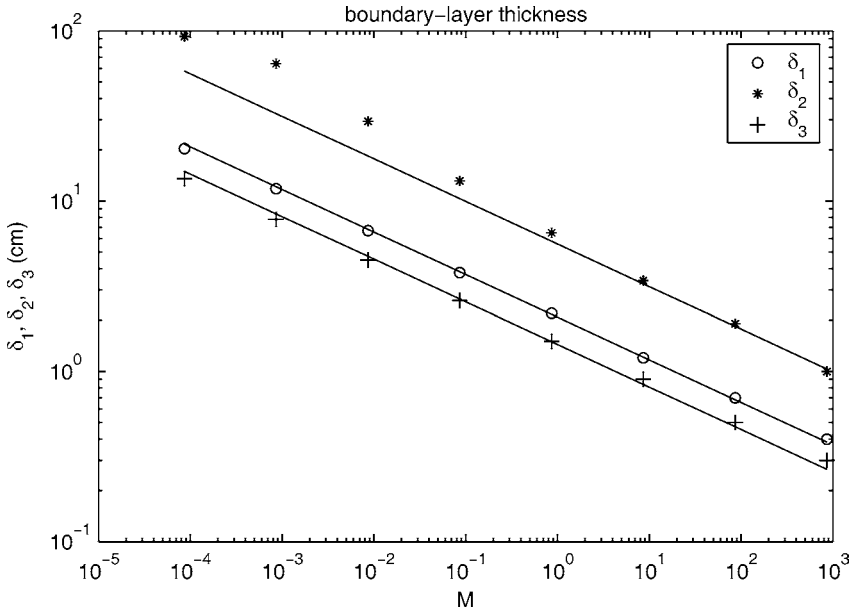

Figure 16. Scaling of the width of the boundary layer with the viscous Lundquist number M. The straight lines are fits to the data points assuming that the δ's are proportional to $M^{-1/4}$. Stress-free boundary conditions are assumed.

extreme values of Ω_t inside the boundary layer for $d = \delta_3$ where $\dot{\Omega}_t(\delta_3) = 0$. Here the dot on top of the Ω_t denotes differentiation with respect to Ω_t's argument.

What already might be inferred from the data given in Table 1 becomes even more conspicuous from Fig. 16 where the boundary-layer thicknesses δ_1, δ_2, and δ_3 are plotted double logarithmically against the viscous Lundquist number M. It is unmistakable that the various data points, at least for sufficiently large M-values, are on a straight line the slope of which is $-1/4$. In fact the solid, straight lines in Fig. 16 are fits through the data points presuming that the δ's are proportional to $M^{-1/4}$. Obviously the width, say δ, of the viscous boundary layer that is developing along the wall of the torus when viscosity is lowered scales as

$$\delta = O(\nu^{1/4}), \quad \nu \to 0. \tag{13}$$

Along the same lines we show in Fig. 17 the data points for the root mean square values of the poloidal and toroidal velocities at the wall and of the extreme toroidal vorticity inside the boundary layer. The solid, straight lines are once again fits through the data points assuming that both velocity components are proportional to $M^{1/4}$ and that the toroidal vorticity is proportional to the square root of M. Evidently V_p and V_t both scale as $O(\nu^{-1/4})$ whereas Ω_t scales as $O(\nu^{-1/2})$ as $\nu \to 0$ and inside the boundary layer. Right on the wall of the torus, i.e. for $d = 0$, the toroidal vorticity can be shown to be $O(\nu^{-1/4})$ for $\nu \to 0$.

In summary, the overall picture of the viscous boundary layer that develops when viscosity of the plasma becomes smaller and smaller is one in which increasingly large flow speeds (scaling as $O(\nu^{-1/4})$) develop and where a mono-layer of increasingly strong toroidal vorticity (scaling as $O(\nu^{-1/2})$) is covering the wall of the torus. The poloidal velocity stream function ψ on the other hand remains finite

https://doi.org/10.1017/S0022377803002629 Published online by Cambridge University Press

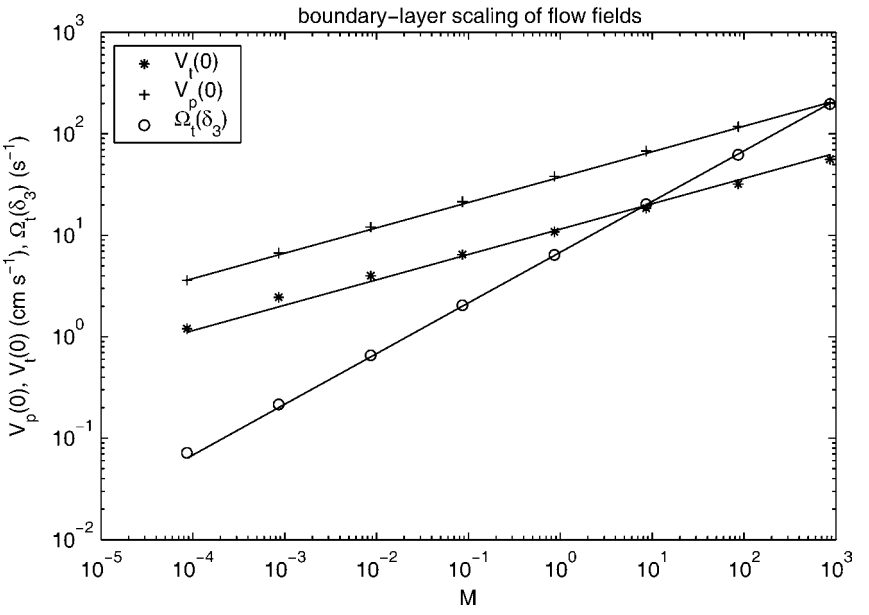

Figure 17. Scaling of the mechanical variables inside the boundary layer with the viscous Lundquist number M. The straight lines are fits to the data points assuming that both velocity components are proportional to $M^{1/4}$ and the toroidal vorticity is proportional to $M^{1/2}$. Stress-free boundary conditions are assumed.

for decreasing viscosity. The latter is in agreement with the Poisson-like equation (A 7) that relates this stream function to the toroidal vorticity. From (13) we learn that the left-hand side of (A 7) scales as $\mathrm{O}(\nu^{-1/2})$, which is identical to the scaling of the right-hand side.

Replacing the gradient operator ∇ by $\nu^{-1/4}\tilde{\nabla}$ and the modified Laplace operator Δ^* by $\nu^{-1/2}\tilde{\Delta}^*$ in equations (A 9), (A 10), (A 12), and (A 14) and as far as they act upon the mechanical variables ψ, ω_φ, and v_φ (there is no boundary-layer behaviour in the electromagnetic variables), using the above scaling of these variables and taking the limit of $\nu \to 0$ leaves us to lowest order with the following set of reduced equations valid inside the boundary layer:

$$\begin{aligned} \nabla\omega_\varphi \times \nabla\psi &= 0, \\ \nabla v_\varphi \times \nabla\chi &= 0, \\ \nabla\psi \times \nabla v_\varphi &= 0, \\ \nabla\chi \times \nabla\psi &= 0. \end{aligned} \tag{14}$$

Hence, inside the viscous boundary layer, lines of constant toroidal vorticity, poloidal velocity stream lines, and lines of constant toroidal velocity all tend to line up with the poloidal magnetic field as viscosity is lowered. It has in fact been verified numerically that although ψ, ω_φ, and v_φ develop sharp changes close to the wall of the torus when viscosity is lowered, the Jacobians (as defined by (A 27)) that follow from (14), i.e. $[u_1, u_2]$, $[u_4, u_5]$, $[u_1, u_4]$, and $[u_1, u_5]$, do not. Also, probably as to be expected, the electromagnetic variables B_φ, χ, and Φ do not exhibit any

https://doi.org/10.1017/S0022377803002629 Published online by Cambridge University Press

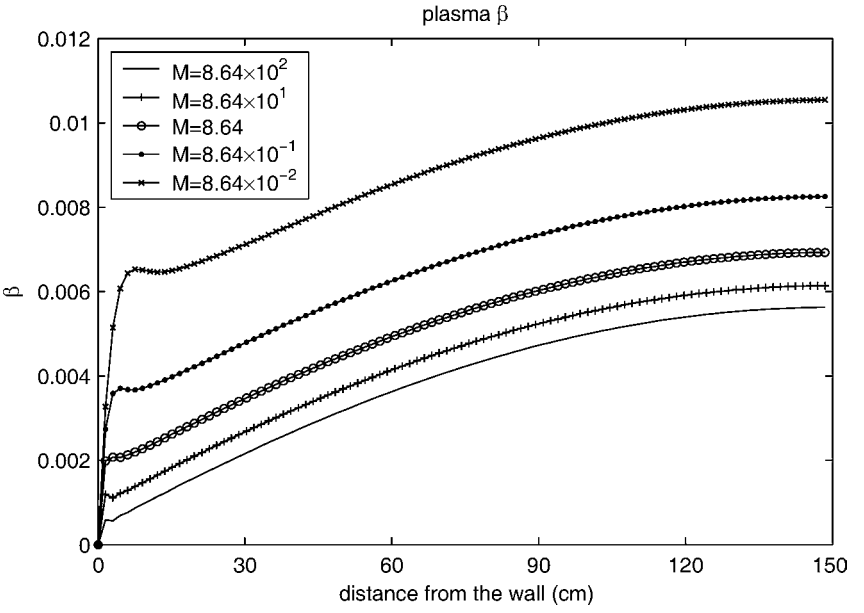

Figure 18. Ratio of mean kinetic pressure p at a certain distance from the wall of the torus and the cross-section averaged magnetic pressure $\langle \|\mathbf{B}\|^2/2 \rangle$, i.e. the plasma β. Stress-free boundary conditions are assumed.

of the boundary-layer behaviour that becomes so prominent in the mechanical variables as the viscosity is scaled down. There is a subtle distinction to be added to the latter remark. Although the total electric current density $\mathbf{J}$ and the total magnetic field $\mathbf{B}$ do not exhibit the above-described boundary-layer behaviour, the angle between these two vectors, that is to say $\|\mathbf{J} \times \mathbf{B}\|/(\|\mathbf{J}\| \, \|\mathbf{B}\|)$, does. The steady states we describe here are primarily force-free in the interior of the torus ($\|\mathbf{J} \times \mathbf{B}\| \ll (\|\mathbf{J}\| \, \|\mathbf{B}\|)$). However, in the boundary layer the angle between $\mathbf{J}$ and $\mathbf{B}$ shows a rapid increase meaning that there these vectors are no longer quasi-parallel any more. The boundary layer is not approximately force-free and steep pressure drops develop inside it. The wall itself is almost an isobar in the sense that the component of ∇p parallel to the wall is much smaller than the normal component of ∇p. Figure 18 shows a plot of the ratio of the pressure p averaged over the circle $(r - r_0)^2 + z^2 = (1 - d/L)^2$ and the cross-section averaged magnetic pressure $\langle \|\mathbf{B}\|^2/2 \rangle$, that is the plasma β as a function of the distance d from the wall of the torus. Note the steep pressure gradient near the wall inside the boundary layer. The resulting pressure gradient force is balanced mainly by the $\mathbf{J} \times \mathbf{B}$ force. The force balance between ∇p and $\mathbf{J} \times \mathbf{B}$ is effective, of course, only in the poloidal directions r and z. There is no toroidal pressure gradient component, and the tiny toroidal component of $\mathbf{J} \times \mathbf{B}$ is balanced by the velocity-dependent terms. Indeed, it is the need to balance the toroidal component of the $\mathbf{J} \times \mathbf{B}$ force that is the most important source of the velocity fields; they are not needed in straight-cylinder geometry.

For the values of the viscous Lundquist number considered in this paper the pressure gradient force is balanced mainly by the $\mathbf{J} \times \mathbf{B}$ force. Throughout the whole torus (including the boundary layer) the other terms in the equation of motion (1)

https://doi.org/10.1017/S0022377803002629 Published online by Cambridge University Press

that involve the velocity of the plasma are much smaller than $\|\mathbf{J} \times \mathbf{B}\|$. From the scaling within the boundary layer one may expect that for sufficiently low viscosity ∇p eventually is going to be balanced by the term $(\mathbf{v} \cdot \nabla)\mathbf{v}$ and/or the term $\nu \nabla^2 \mathbf{v}$. However, MHD itself will break down over the thin boundary layers that result for those extremely low viscosities. Moreover, there is no reason not to expect that like fluid-mechanical states, our MHD states also tend to go unstable and turbulent when the Reynolds-like number M gets large.

We conclude this section with some remarks concerning the no-slip boundary condition. Along the same line as above for the stress-free case we have analysed the behaviour of the boundary layer if all velocities are required to become zero at the wall. It turns out that the width of the boundary layer and the magnitude of the mechanical variables inside it are still governed by the same scaling laws that are found for the stress-free boundary condition (see (13)). As in the case of the stress-free boundary conditions the characteristic flow pattern that emerges for no-slip boundary conditions is once again a pair of counter-rotating poloidal vortices or convection cells and associated with that a toroidal flow that is anti-symmetric with respect to the midplane of the torus, resulting in a net toroidal flow that is nil. For the stress-free boundary case the latter seems to be a probably unstable balance between the toroidal component of $\mathbf{J} \times \mathbf{B}$ and the viscous drag of the magnetofluid (note that there is no component of the pressure gradient in the toroidal direction since this would result in a multi-valued pressure). There is no viscous drag on the wall and therefore it must be that the top half of the plasma is just dragging against the bottom half, and *vice versa*. It therefore might be expected that departures from up–down symmetry of the toroidal geometry could result in a net flow of plasma in one toroidal direction or the other. This possibility will be confirmed in the considerations of Sec. 4, involving asymmetrical cross sections.

4. An asymmetric cross section

In the present section we demonstrate that the dipolar flow pattern in a poloidal plane that is so characteristic for a cross section that is symmetric about the major axis of the torus (see Montgomery and Shan 1994; Montgomery et al. 1997b; Kamp et al. 1998; Bates and Montgomery 1998; Montgomery et al. 1999; Kamp and Montgomery 2003) goes to a monopolar flow pattern when the cross section becomes 'D'-shaped (see Fig. 1(b)) and stress-free boundary conditions are imposed.

Figures 19–24 show the evolution of the poloidal and toroidal flow patterns when the stress-free boundary conditions are assumed and the viscous Lundquist number M is increased in two steps from its lower-bound value $M = M_{\mathrm{low}} = 8.64 \times 10^{-5}$ to $M = 10^6 \times M_{\mathrm{low}}$ keeping all other parameters constant. What becomes apparent immediately from these plots is that as the viscosity is lowered, the character of the poloidal flow pattern more and more tends to become monopolar. One convection cell becomes dominant over the other one by pushing the latter towards the wall of the torus (see Figs. 21 and 23). Although there still is flow in the positive as well as negative toroidal directions, there is a net mass flow in the toroidal direction that is not zero as for the symmetrical cross section. In most parts of the present 'D'-shaped cross section the toroidal flow is in the negative φ-direction with speeds in excess of $300\,\mathrm{cm\,s^{-1}}$ for $M = 86.4$. A better indication for the net toroidal mass flow is obtained by considering values of v_φ that are averaged over the cross section of the torus. In Table 2 we show these mean (dimensional) values of the toroidal

https://doi.org/10.1017/S0022377803002629 Published online by Cambridge University Press

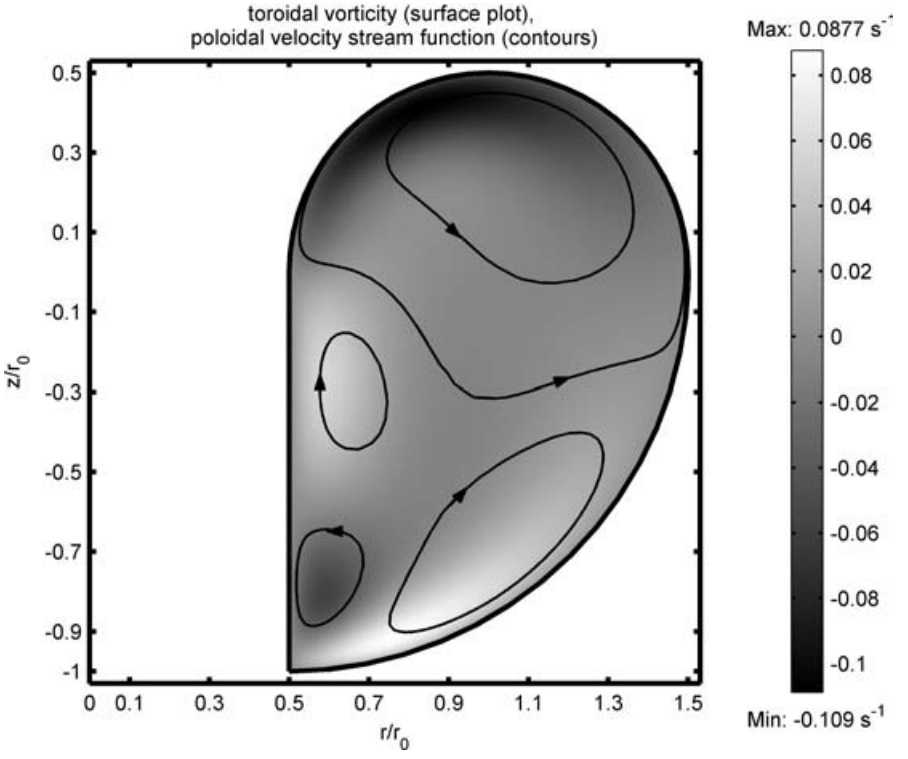

Figure 19. Surface plot of the (dimensional) toroidal vorticity ω_φ combined with contours of the poloidal velocity stream function ψ with $M = 8.64 \times 10^{-5}$. The grey-scale bar indicates the dimensional value of the toroidal vorticity in s^{-1}. Stress-free boundary conditions are assumed.

Table 2. Toroidal velocity averaged over the cross section of the torus.

M	$\langle v_\varphi \rangle$ (cm s^{-1})	$(\langle \Vert \mathbf{v}_{\mathrm{poloidal}} \Vert^2 \rangle)^{1/2}$ (cm s^{-1})
8.64×10^{-9}	1×10^{-6}	0.003
8.64×10^{-7}	6×10^{-4}	0.2
8.64×10^{-5}	3	0.7
8.64×10^{-4}	−8	1.0
8.64×10^{-3}	−11	1.3
8.64×10^{-2}	−17	1.7
8.64×10^{-1}	−28	2.2
8.64×10^{0}	−48	3.0
8.64×10^{1}	−83	4.1
8.64×10^{2}	−144	5.5

speed for various values of the viscous Lundquist number. For the highest M-value considered here, it would take approximately 15 s for a plasma element to encircle the torus. In Fig. 25 we show stream lines of the combined poloidal and toroidal flow fields for $M = 8.64$ and stress-free boundary conditions. The net mass flow that is so apparent in this plot is lost whenever no-slip rather than stress-free

https://doi.org/10.1017/S0022377803002629 Published online by Cambridge University Press

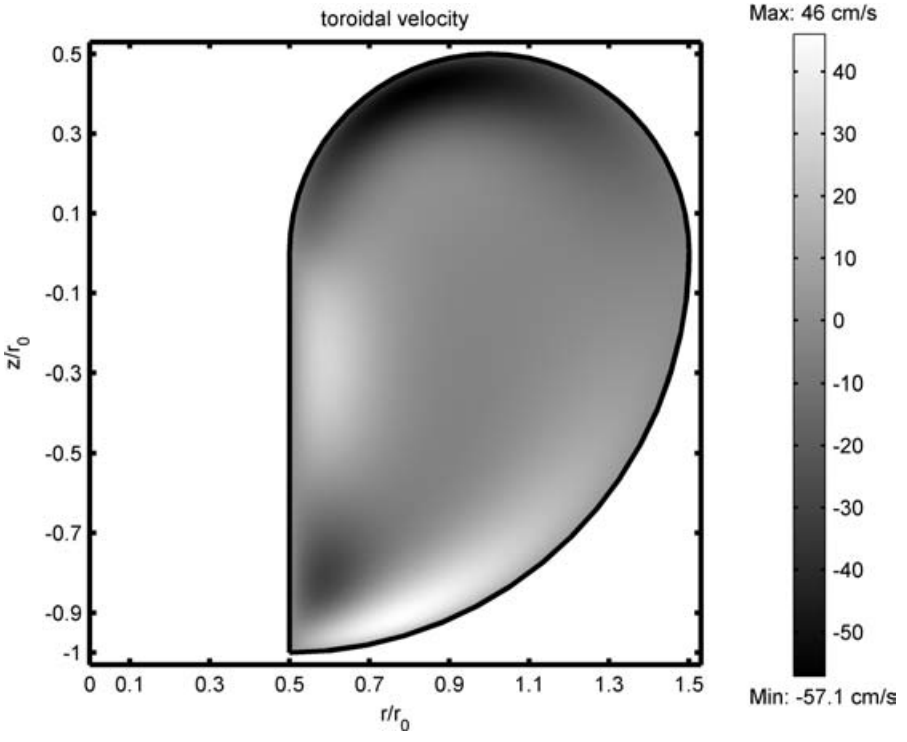

Figure 20. Surface plot of the (dimensional) toroidal velocity v_φ with $M = 8.64 \times 10^{-5}$. The grey-scale bar indicates the dimensional value of the toroidal velocity in $\mathrm{cm\,s^{-1}}$. Stress-free boundary conditions are assumed.

boundary conditions are imposed. In Fig. 26 we also show the stream lines of the combined poloidal and toroidal flow fields inside the torus but now for no-slip boundary conditions (the viscous Lundquist number is again 8.64). The net flow in the toroidal direction is in the latter case practically zero and stays more or less zero even if the viscosity is lowered further, as has been verified numerically.

5. Discussion and conclusions

The flows reported here have something in common with Hartmann flow (e.g. Davidson 2001), though the work being done here is done Ohmically rather than mechanically, and the velocity field remains energetically quite small compared to the energy in the magnetic fields. Hartmann flow is also characterized by steep boundary layers at low viscosity. The geometry is intrinsically more complicated and the scaling is quite different than in Hartmann flow, however, and so far we have not seen how to extract analytical expressions for the behaviour of the boundary layer discovered numerically as is possible for the Hartmann flow case. A systematic asymptotic analysis of the boundary-layer behaviour seems a valid goal for the future.

The other new interesting feature to have emerged is the sensitivity of the flow pattern to the poloidal boundary shape and boundary conditions imposed there. In light of fluid dynamic precedents, this is perhaps not surprising, but it has not been

https://doi.org/10.1017/S0022377803002629 Published online by Cambridge University Press

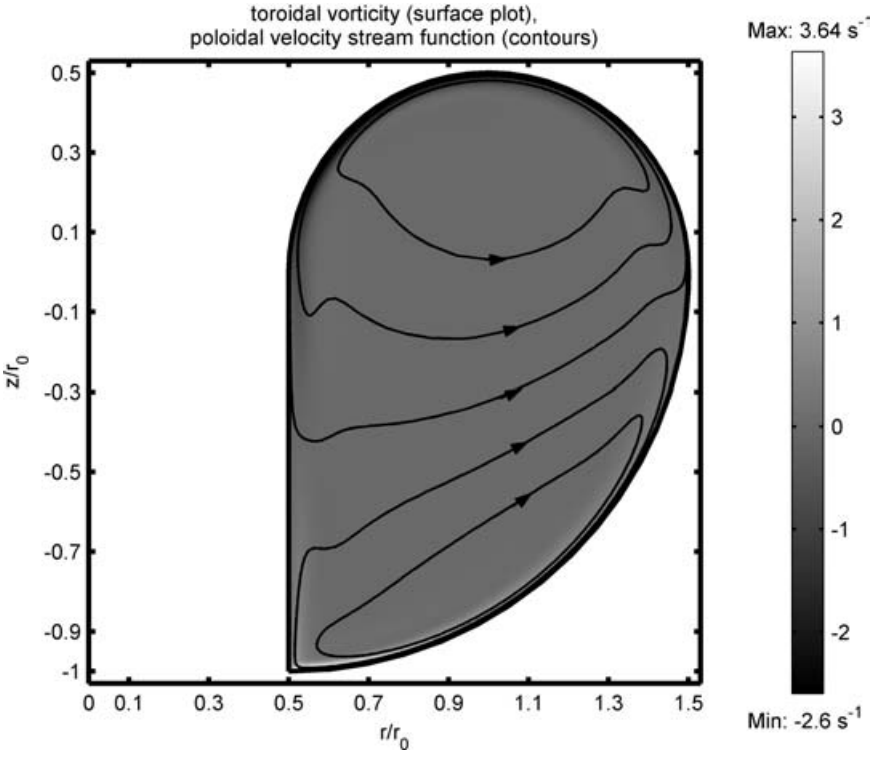

Figure 21. Same as Fig. 19 but with $M = 8.64 \times 10^{-2}$.

typically a feature of earlier discussions of MHD equilibria, almost all of which have been in the ideal MHD framework. Our previous investigations involved cross sections (rectangular or circular) that were symmetric about the midplane $z = 0$, and we had endowed the dipolar 'double smoke ring' pattern that characterizes that situation with more universality than it deserves, as seen in Figs. 19–24. We should remark that some discussions of 'zonal flow', electrostatic in character, have appeared in the tokamak literature, but usually without an attempt to draw a global weather map of the flow pattern. Indeed, all confined steady-state flows must be 'zonal' in some sense, and it seems to us most important to characterize the entire, global character of the flow, in light of the fact that it differs so much from one point to another inside the toroid. Experimentally, the ability to characterize the flow in a tokamak at all spatial points seems far in the future, though no fundamental obstacles would appear to exist if such measurements came to seem desirable enough. The reason for desiring them seems to us to be that the stability properties of the MHD steady states, on which so much of the fusion literature is based, are likely to be affected by the presence of flows of the kind encountered here.

Several features of the calculation remain troublesome, most notably the absence of information, experimental and theoretical, as just how to represent the viscous effects in a tractable way and what numerical values to assign the viscosity coefficients. It is also a serious restriction to be committed to incompressible flows.

https://doi.org/10.1017/S0022377803002629 Published online by Cambridge University Press

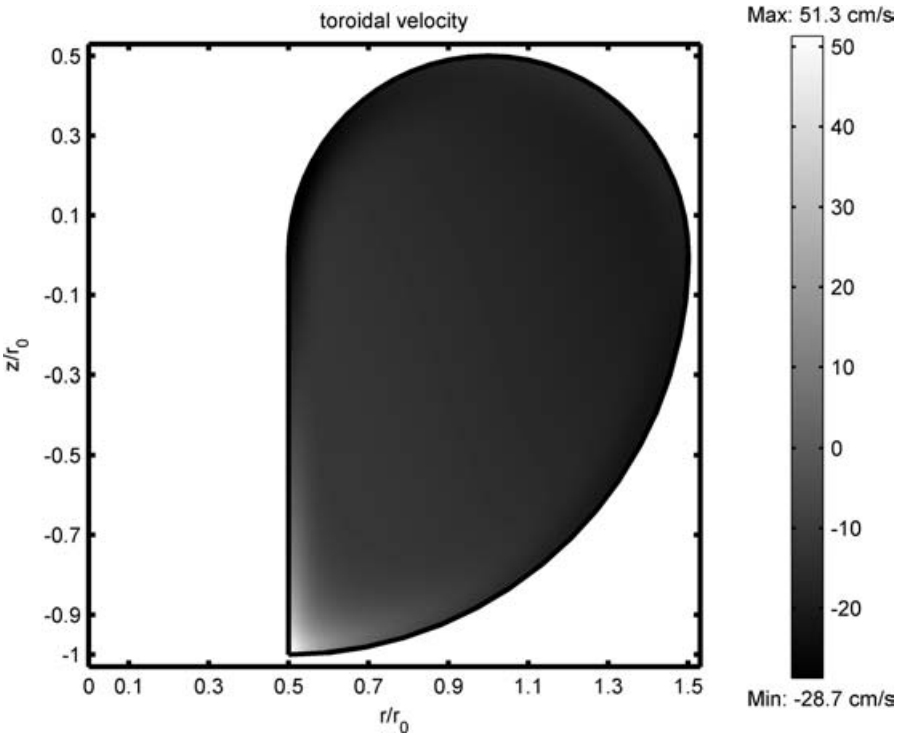

Figure 22. Same as Fig. 20 but with $M = 8.64 \times 10^{-2}$.

Finally, the assumption of axisymmetry itself is an uneasy one, because of the slots and slits in the conducting boundary that are necessary to admit all the imaginable driving mechanisms such as the toroidal electric field assumed here. It is to be hoped that ways will be seen to move beyond these three limitations. Even then, the inevitable gaps between fusion plasma dynamics and the MHD approximation will remain, but they should be far smaller than those between ideal MHD and real fusion plasmas.

Appendix. Equations to be solved

In this appendix we rewrite the set of non-ideal MHD equations (1) through (6) into a set of coupled partial differential equations and formulate boundary conditions to be imposed on the solutions of these equations for a torus the wall of which can either not sustain any tangential viscous stress or is no-slip. Since the steady states to be found are assumed to be axisymmetric, we introduce scalar variables according to

$$\mathbf{v}(r,z) = \nabla\psi \times \nabla\varphi + v_\varphi \hat{\mathbf{i}}_\varphi, \tag{A 1}$$

$$\mathbf{B}(r,z) = \nabla\chi \times \nabla\varphi + \left(B_0 \frac{r_0}{r} + B_\varphi\right) \hat{\mathbf{i}}_\varphi, \tag{A 2}$$

where ψ is the stream function and χ is the flux function. Since there is no time dependence, the gradient of a scalar field may be added to the externally applied

https://doi.org/10.1017/S0022377803002629 Published online by Cambridge University Press

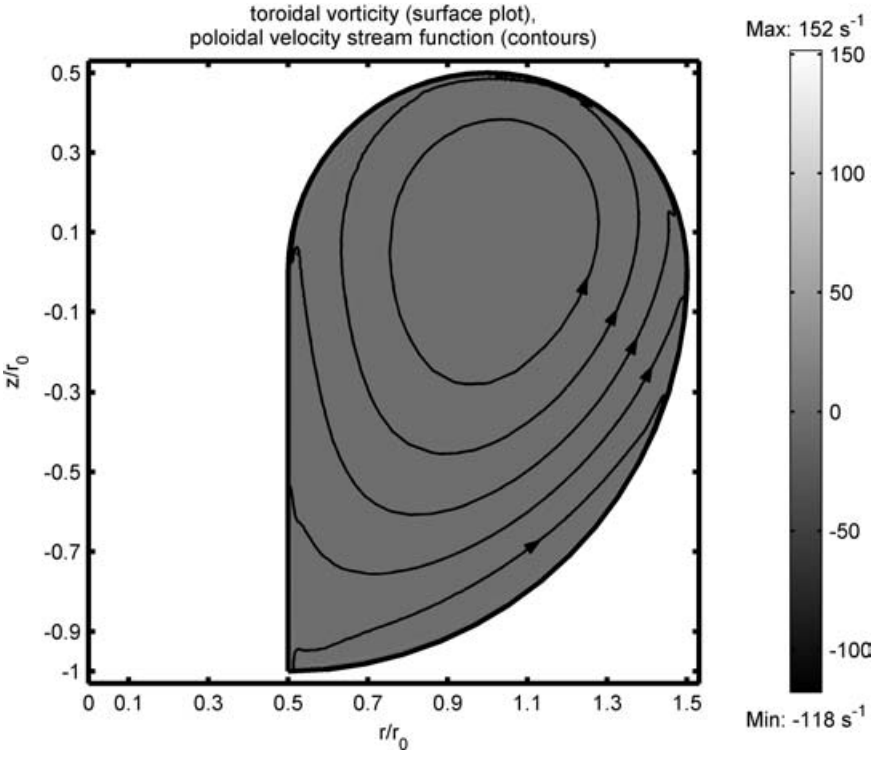

Figure 23. Same as Fig. 19 but with $M = 86.4$.

electric field,

$$\mathbf{E}(r,z) = E_0 \frac{r_0}{r}\hat{\mathbf{i}}_\varphi - \nabla\Phi. \tag{A 3}$$

With these new variables the electric current density $\mathbf{J}$ and the vorticity $\boldsymbol{\omega} = \nabla \times \mathbf{v}$ may be expressed as

$$\mathbf{J}(r,z) = \nabla(rB_\varphi) \times \nabla\varphi - \nabla^2(\chi\nabla\varphi) = \nabla(rB_\varphi) \times \nabla\varphi - \frac{1}{r}(\Delta^*\chi)\hat{\mathbf{i}}_\varphi, \tag{A 4}$$

$$\boldsymbol{\omega}(r,z) = \nabla(rv_\varphi) \times \nabla\varphi - \nabla^2(\psi\nabla\varphi) = \nabla(rv_\varphi) \times \nabla\varphi - \frac{1}{r}(\Delta^*\psi)\hat{\mathbf{i}}_\varphi, \tag{A 5}$$

where the modified Laplace operator Δ^* is defined by

$$\Delta^* A = \nabla^2 A - \frac{2}{r}\frac{\partial A}{\partial r} = \frac{\partial^2 A}{\partial r^2} - \frac{1}{r}\frac{\partial A}{\partial r} + \frac{\partial^2 A}{\partial z^2}. \tag{A 6}$$

Taking the toroidal part of (A 5) results in

$$\Delta^*\psi = -r\omega_\varphi. \tag{A 7}$$

Next consider the vorticity equation that is obtained from taking the curl of the force-balance equation (1):

$$\nu\nabla^2\boldsymbol{\omega} = \nabla \times (\boldsymbol{\omega} \times \mathbf{v} + \mathbf{J} \times \mathbf{B}). \tag{A 8}$$

https://doi.org/10.1017/S0022377803002629 Published online by Cambridge University Press

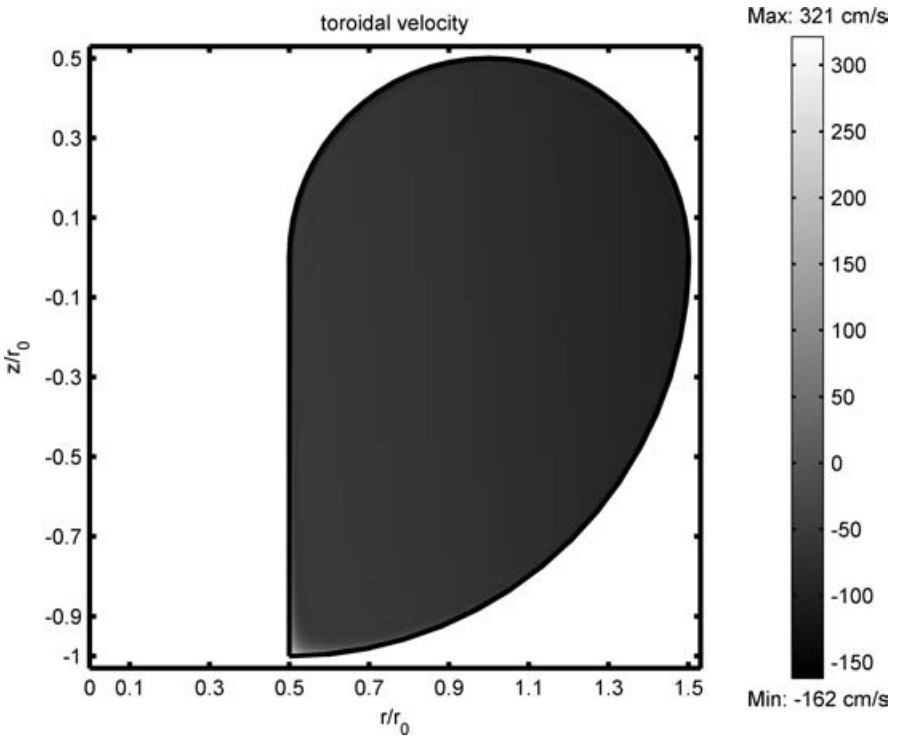

Figure 24. Same as Fig. 20 but with $M = 86.4$.

Taking the toroidal part of this equation yields

$$\nu\Delta^*(r\omega_\varphi)\nabla\varphi = \nabla(rv_\varphi)\times\nabla\left(\frac{v_\varphi}{r}\right) + \nabla\left(\frac{\omega_\varphi}{r}\right)\times\nabla(\psi) + \nabla\left(\frac{B_\varphi}{r}+\frac{B_0 r_0}{r^2}\right)\times\nabla(rB_\varphi) + \nabla\chi\times\nabla\left(\frac{J_\varphi}{r}\right). \tag{A 9}$$

The curl of the poloidal part of Ohm's law (2) leads to the following equation for B_φ:

$$\eta\Delta^*(rB_\varphi)\nabla\varphi = \nabla\left(\frac{B_\varphi}{r}+\frac{B_0 r_0}{r^2}\right)\times\nabla\psi - \nabla\left(\frac{v_\varphi}{r}\right)\times\nabla\chi. \tag{A 10}$$

An equation for v_φ is obtained by rewriting the force-balance equation (1) as follows:

$$\nu\nabla^2\mathbf{v} = \nabla\left(p+\tfrac{1}{2}v^2\right) + \boldsymbol{\omega}\times\mathbf{v} - \mathbf{J}\times\mathbf{B}. \tag{A 11}$$

The toroidal part of this equation gives

$$\nu\Delta^*(rv_\varphi) = [\nabla\chi\times\nabla(rB_\varphi) - \nabla\psi\times\nabla(rv_\varphi)]\cdot\nabla\varphi. \tag{A 12}$$

The toroidal part of (A 4) results in

$$\Delta^*\chi = -rJ_\varphi, \tag{A 13}$$

where the toroidal current density follows from the toroidal part of Ohm's law,

$$\eta r J_\varphi = E_0\frac{r_0}{r} - \frac{\nabla\chi\times\nabla\psi}{r}\cdot\nabla\varphi. \tag{A 14}$$

https://doi.org/10.1017/S0022377803002629 Published online by Cambridge University Press

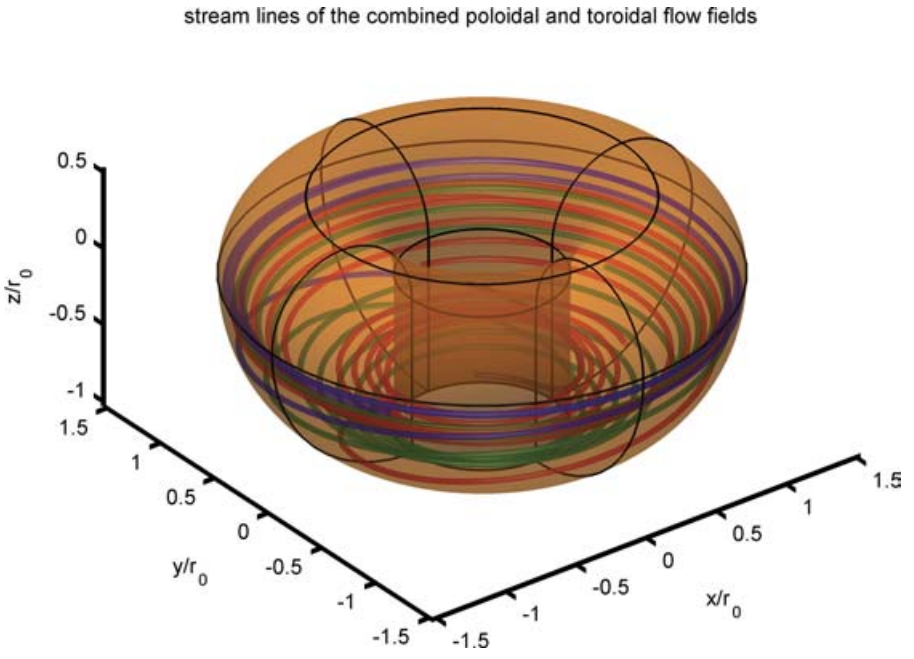

Figure 25. Three stream lines of the total, i.e. the combined poloidal and toroidal flow fields, when stress-free boundary conditions are imposed and $M = 8.64$.

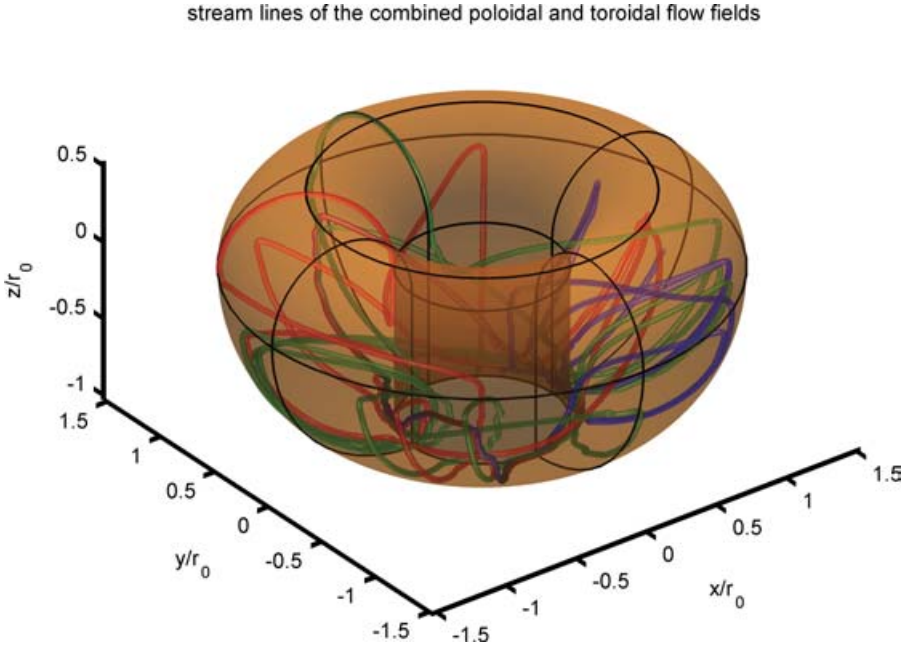

Figure 26. Same as Fig. 25 but with no-slip boundary conditions imposed.

https://doi.org/10.1017/S0022377803002629 Published online by Cambridge University Press

The equations (A 7), (A 9), (A 10), (A 12), and (A 13) form a set of coupled, non-linear Poisson-like equations for the scalar variables ψ, $r\omega_\varphi$, rB_φ, rv_φ, and χ to be supplemented with expression (A 14) for J_φ. Note that these equations can be solved without *a priori* knowing the pressure p and the scalar potential Φ. Once this is done ∇p follows from the force-balance equation (1) rewritten as follows,

$$\nabla p = \nu\nabla^2\mathbf{v} - \nabla\left(\frac{v^2}{2}\right) - \boldsymbol{\omega}\times\mathbf{v} + \mathbf{J}\times\mathbf{B}. \tag{A 15}$$

This determines the pressure up to an additive constant. In a similar fashion Φ follows from the poloidal part of Ohm's law, i.e.

$$\nabla\Phi = \mathbf{v}\times\mathbf{B} - \eta\nabla(rB_\varphi)\times\nabla\varphi, \tag{A 16}$$

in which we have used Ampère's law (3) to replace the poloidal current density in terms of the toroidal magnetic field.

The final step is to introduce new variables according to

$$\begin{aligned} u_1 &= \frac{\psi}{r_0}, \quad u_2 = r_0 r\omega_\varphi, \quad u_3 = \frac{rB_\varphi}{I_\mathrm{b}} + 1, \\ u_4 &= \frac{rv_\varphi}{I_\mathrm{b}}, \quad u_5 = \frac{\chi}{r_0}, \quad u_6 = r_0 rJ_\varphi - I_e, \end{aligned} \tag{A 17}$$

where

$$I_e = Sr_0^2E_0 \quad \text{and} \quad I_\mathrm{b} = r_0B_0, \tag{A 18}$$

and

$$x = \frac{r}{r_0}, \quad y = \frac{z}{r_0}. \tag{A 19}$$

In terms of these new variables the partial differential equations (A 7), (A 9), (A 10), (A 12), (A 13), and (A 14) become respectively

$$\Delta^* u_1 = -u_2, \tag{A 20}$$

$$\frac{1}{M}\Delta^* u_2 = \frac{I_\mathrm{b}^2}{x^2}\frac{\partial}{\partial y}(u_3^2 - u_4^2) + \frac{2}{x^2}\left\{u_2\frac{\partial u_1}{\partial y} - (u_6 + I_e)\frac{\partial u_5}{\partial y}\right\} + \frac{1}{x}([u_1, u_2] - [u_5, u_6]), \tag{A 21}$$

$$\frac{1}{S}\Delta^* u_3 = \frac{2}{x^2}\left(u_3\frac{\partial u_1}{\partial y} - u_4\frac{\partial u_5}{\partial y}\right) + \frac{1}{x}([u_1, u_3] + [u_4, u_5]), \tag{A 22}$$

$$\frac{1}{M}\Delta^* u_4 = \frac{1}{x}([u_3, u_5] + [u_1, u_4]), \tag{A 23}$$

$$\Delta^* u_5 = -(u_6 + I_e), \tag{A 24}$$

$$\frac{1}{S}u_6 = \frac{1}{x}[u_5, u_1], \tag{A 25}$$

where now the operator Δ^* is to be read as

$$\Delta^* A = \nabla^2 A - \frac{2}{x}\frac{\partial A}{\partial x} = \frac{\partial^2 A}{\partial x^2} - \frac{1}{x}\frac{\partial A}{\partial x} + \frac{\partial^2 A}{\partial y^2}. \tag{A 26}$$

https://doi.org/10.1017/S0022377803002629 Published online by Cambridge University Press

In the above equations $[u, v]$ denotes the Jacobian bracket of two functions u and v with respect to the variables x and y that is defined as

$$[u, v] = \frac{\partial u}{\partial x}\frac{\partial v}{\partial y} - \frac{\partial u}{\partial y}\frac{\partial v}{\partial x}. \tag{A 27}$$

For the circular cross section as is considered in Sec. 3, the computational demand for solving (A 20)–(A 25) can be halved using obvious symmetries in the variables with respect to the midplane of the torus. If the numerics is restricted to the upper half of the torus, we need boundary conditions for $z = 0$ and for the upper semicircle of the cross section. Based on the oddness or evenness of the variables in that case, we can formulate the following boundary conditions for $z = 0$:

$$\left.\frac{\partial B_\varphi}{\partial z}\right|_{z=0} = 0, \quad \left.\frac{\partial J_\varphi}{\partial z}\right|_{z=0} = 0, \quad \left.\frac{\partial \chi}{\partial z}\right|_{z=0} = 0,$$
$$\psi|_{z=0} = 0, \quad \omega_\varphi|_{z=0} = 0, \quad v_\varphi|_{z=0} = 0. \tag{A 28}$$

For the remaining part of the boundary of the circular cross section as used in Sec. 3, we either choose stress-free mechanical boundary conditions, that is

$$\psi|_{\text{semicircle}} = 0, \quad \left.\frac{\partial \psi}{\partial n}\right|_{\text{semicircle}} = -\frac{r_0 r}{4}\omega_\varphi|_{\text{semicircle}},$$
$$\left.\frac{\partial v_\varphi}{\partial n}\right|_{\text{semicircle}} = 2\frac{r - r_0}{r_0 r}v_\varphi|_{\text{semicircle}}, \tag{A 29}$$

or no-slip mechanical boundary conditions, that is

$$\psi|_{\text{semicircle}} = 0 = \left.\frac{\partial \psi}{\partial n}\right|_{\text{semicircle}},$$
$$v_\varphi|_{\text{semicircle}} = 0, \tag{A 30}$$

where $\partial/\partial n$ denotes the outward normal derivative. In both cases the electromagnetic variables need to satisfy at the semicircle:

$$B_\varphi|_{\text{semicircle}} = 0 = \chi|_{\text{semicircle}},$$
$$J_\varphi|_{\text{semicircle}} = SE_0\left.\frac{r_0}{r}\right|_{\text{semicircle}}. \tag{A 31}$$

The latter condition is implied by the fact that the toroidal component of the $\mathbf{v} \times \mathbf{B}$ term in Ohm's law should vanish at the wall of the torus.

Obviously the above-described reduction in the computational effort is not an option any more when considering an asymmetric cross section as is done in Sec. 4. For the torus that is depicted in Fig. 1(b) the numerical computations have to be performed in the whole 'D'-shaped cross section. When considering stress-free boundary conditions, we need to satisfy:

- for the straight-line element denoted by I in Fig. 1(b)

$$\psi|_{\text{I}} = 0 = \omega_\varphi|_{\text{I}}, \quad \left.\frac{\partial}{\partial r}\left(\frac{v_\varphi}{r}\right)\right|_{\text{I}} = 0, \tag{A 32}$$

https://doi.org/10.1017/S0022377803002629 Published online by Cambridge University Press

• for the semicircle denoted by II in Fig. 1(b), the stress-free boundary conditions are in fact given by (A 29) and last for the quarter-circle denoted by III in Fig. 1(b)

$$\begin{aligned} \psi|_{\mathrm{III}} &= 0, \\ \left.\frac{\partial\psi}{\partial n}\right|_{\mathrm{III}} &= -\frac{r_0 r}{2}\omega_\varphi|_{\mathrm{III}}, \\ \left.\frac{\partial v_\varphi}{\partial n}\right|_{\mathrm{III}} &= \frac{2r - r_0}{2r_0 r}v_\varphi|_{\mathrm{III}}. \end{aligned} \tag{A 33}$$

When imposing no-slip boundary conditions, we need to satisfy at the 'D'-shaped wall

$$\begin{aligned} \psi|_{\mathrm{wall}} = 0 = \left.\frac{\partial\psi}{\partial n}\right|_{\mathrm{wall}}, \\ v_\varphi|_{\mathrm{wall}} = 0. \end{aligned} \tag{A 34}$$

As for the circular cross section the electromagnetic variables need to satisfy for the asymmetric, 'D'-shaped cross section in both cases

$$\begin{aligned} B_\varphi|_{\mathrm{wall}} = 0 = \chi|_{\mathrm{wall}}, \\ J_\varphi|_{\mathrm{wall}} = SE_0\left.\frac{r_0}{r}\right|_{\mathrm{wall}}. \end{aligned} \tag{A 35}$$

We finally note that the above boundary conditions can be reformulated straightforwardly in terms of either Dirichlet or Neumann boundary conditions to be imposed upon the numerical variables u_1, u_2, u_3, u_4, u_5 and u_6.

References

Balescu, R. 1988 *Transport Processes in Plasmas*, Vol. I. Amsterdam: North-Holland, pp. 247 ff.

Bateman, G. 1978 *MHD Instabilities*. Cambridge: MIT Press.

Bates, J. W. and Lewis, H. R. 1996 A toroidal boundary-value problem in resistive magnetohydrodynamics. *Phys. Plasmas* **3**, 2395–2400.

Bates, J. W. and Montgomery, D. C. 1998 Toroidal visco-resistive magnetohydrodynamic steady states contain vortices. *Phys. Plasmas* **5**, 2649–2653.

Book, D. L. 1987 *The NRL Plasma Formulary*. Washington: U.S. Naval Research Laboratory Publication 0084-4040.

Braginskii, S. I. 1965 Transport processes in a plasma. In: *Reviews of Plasma Physics*, Vol. 1 (ed. M. A. Leontovich). London: Consultants Bureau, pp. 205–311.

Cowling, T. G. 1958 *Magnetohydrodynamics*. London: Interscience.

Davidson, P. A. 2001. *An Introduction to Magnetohydrodynamics*. Cambridge: Cambridge University Press, pp. 151–153.

FEMLAB Reference Manual 2001 version 2.2. COMSOL AB, Stockholm, Sweden.

Grad, H. 1967 Toroidal containment of a plasma. *Phys. Fluids* **10**, 137–154.

Grad, H. and Hogan, J. 1970 Classical diffusion in a tokomak. *Phys. Rev. Lett.* **24**, 1337–1340.

Grad, H., Hu, P. N., Stevens, D. C. and Turkel E. 1977 Classical plasma diffusion. In: *Plasma Physics and Controlled Fusion Research*. Paper IAEN-CN-35/B9, Vol. II. International Atomic Energy Agency, pp. 355–367.

JET team 1992 Fusion energy production from a deuterium–tritium plasma in the JET tokamak. *Nucl. Fusion* **32**, 187–203.

Kamp, L. P. and Montgomery, D. C. 2003 Toroidal flows in resistive magnetohydrodynamic steady states. *Phys. Plasmas* **10**, 157–167.

Kamp, L. P., Montgomery, D. C. and Bates J. W. 1998 Toroidal flows in resistive magnetohydrodynamic steady states. *Phys. Fluids* **10**, 1757–1766.

Montgomery, D. C., Bates, J. W. and Kamp, L. P. 1999 MHD steady states as a model for confined plasmas. *Plasma Phys. Control. Fusion* **41**, A507–A517.

Montgomery, D. C., Bates, J. W. and Lewis, H. R. 1997a Resistive magnetohydrodynamic equilibria in a torus. *Phys. Plasmas* **4**, 1080–1086.

Montgomery, D. C., Bates, J. W. and Li S. 1997b Toroidal vortices in resistive magnetohydrodynamic equilibria. *Phys. Fluids* **9**, 1188–1193.

Montgomery, D. and Shan, X. 1994 Toroidal resistive MHD equilibria. *Commun. Plasma Phys. Control. Fusion* **15**, 315–320.

Pfirsch, D. and Schlüter, A. 1962 Influence of electrical conductivity on the equilibrium of low pressure plasmas in stellerators. In: *Max Planck Institut Report MPI/PA/62*. Copies can be ordered from the National Technical Information Service, 5285 Port Royal Road, Springfield, VA 22161, USA.

Ponno, A., Galgani, G. and Montgomery, D. C. 2002 A class of resistive axisymmetric magnetohydrodynamic equilibria in a periodic cylinder. *J. Plasma Phys.* **4**, 251–269.

Rosen, M. D. and Greene, J. M. 1977 Radial boundary layers in diffusing toroidal equilibria. *Phys. Fluids* **20**, 1446–1475.

Shercliff, J. A. 1965 *A Textbook on Magnetohydrodynamics*. London: Pergamon.

Throumoulopoulos, G. N. and Tasso, H. 2003 On axisymmetric resistive magnetohydrodynamic equilibria with flow free of Pfirsch–Schlüter diffusion. *Phys. Plasmas* **10**, 2382–2388.

Wesson, J. A. and Campbell, D. J. 1997 *Tokamaks*, 2nd edn. Oxford: Clarendon.